University Review, Vol. 15, Issue 4, p. 1-6, 2021.

UNIVERSITY REVIEW

NANOINDENTATION STUDY OF CHROME LAYER

Maroš Eckert[1*] – Michal Krbaťa[1]

[1]Design and Special Technology Department, Faculty of Special Technology, Alexander Dubcek University of Trencin, Ku kyselke 469, 911 06 Trencin

ARTICLE INFO (10 pt, bold)…filled by the publisher

***Article history*:**
Received: 26.11.2021
Received in revised form: 7.12.2021
Accepted: 13.12.2021

Keywords:
Chrome layer
Nanoindentation
Microhardness
Nanohardness

Abstract:

The article focuses on the analysis of chromium layers applied in various companies on the base material in the form of a tube of AISI 304 material. The measurement of the thickness of the chromium layer was performed by optical microscopy on samples formed by cross section. The quality of the chromium layer was evaluated using two different methods of measuring hardness. One was the classical method of measuring microhardness (Hv0.1) from the surface part of chromium. The second method was nanoindentation analysis, in which the nano-hardness was measured along the thickness of the chromium layer. The results show that the surface hardness has increased more than 3-fold by using a chromium layer. It has also been shown that a layer with greater thickness does not show the greatest microhardness. From the nanoindentation results, it was confirmed that the layer with the highest surface hardness also shows the highest nanoindentation hardness after the layer thickness, and this hardness decreases in the direction away from the surface of the base material in all layers.

1 Introduction

The rapid development of materials physics and its successful application in various industries has led to an increase in requirements for the study of the mechanical properties of thin films. These are quantified, inter alia, by mechanical quantities such as hardness, modulus of elasticity, fracture toughness, stress, viscoelastic parameters, ductility, creep or stiffness. The most used method for the study of local mechanical properties is nanoindentation - indentation with penetration depth in the nanometer scale. This is a relatively simple method, which consists in injecting a material with known mechanical properties with a known force into a material whose mechanical properties are unknown, as shown in Figure 1.5. The advantage is that it is a non-destructive method, and it is possible to determine the mechanical properties of a wide range of materials such as metals, ceramics or alloys [1]. Methods based on measuring the contact area from residual indentation have been used in the past to study mechanical properties. However, since the nanoindentation is performed with small loads, the resulting residual area is very small. That is why it was necessary to replace the light microscope, electron microscope or microscope with a scanning probe, which would greatly complicate the measurement. For this reason, the DSI (Depth-sensing indentation) method was developed, which is based on recording the instantaneous values of the applied force and the depth of indenter formation, from which the contact area can be calculated. The

[*] Corresponding author. Tel.: +421 32 7400 246
E-mail address: maros.eckert@tnuni.sk

measured dependence of the applied force L on the penetration depth h is known as the load-depth curve. Nanoindentation analysis began to be significantly applied in determining the hardness and mechanical properties of thin films, where measurement by standard methods would not be possible. An example of such a layer is electrolytic chromium plating. Chromium is a blue-white and shiny metal resistant to corrosion in most environments. Mainly for its resistance to external influences together with its aesthetic appearance, it is widely used as the last finishing operation for the surface treatment of metal parts [2]. In general, there are two types of chromium plating, namely decorative, in which the thin coating serves as a glossy and durable surface treatment. The second type is industrial or hard chromium, in which it uses a chromium coating for its advantageous properties such as resistance to heat, wear, corrosion and erosion, abrasion and low coefficient of friction. The difference between decorative and hard chrome is not only in the purpose of its use, but also in the different thickness of the chrome layer. In the case of decorative chromium, this layer ranges from 0.5 to 2 μm, in the case of hard chromium, the standard layer thickness is from 10 to 250 μm [3]. The use of hard chromium is used not only on steel, but preferably also on other metallic materials to form a durable surface layer [4]. Electrolytic chromium plating is an important means of extending the life of all types of metal parts that are exposed to wear, friction, abrasion, and corrosion. Such components may have protected functional surfaces with a chromium layer, whereby after wear of such surfaces it is possible to re-form a chromium layer which either immediately or after further processing meets the original properties and tolerances. Because hard chromium has a low surface energy, it is often used on sliding or rotating parts of motors, pumps, compressors and hydraulic or pneumatic piston rods [5]. Another advantage is its high corrosion resistance, which makes it widely used to protect the surfaces of parts exposed to various highly corrosive environments [6]. Another advantage is that the chromium plating process is relatively cold and can therefore be used to increase the hardness of the surfaces of very small parts without the risk of thermal deformation or a change in the properties of the base material. Hard chromium coatings achieve a hardness in the range of 56 to 74 HRC depending on the electrolytic bath used. In most cases, the greater the hardness, the longer the life of the component. Therefore, it is best to use a plating process that provides the highest hardness. A component with a hardness of up to 70 HRC will provide the longest possible service life. Decorative chrome plating provides the same hardness values as industrial chromium, but these tend to be harder only for a thicker layer of chrome. For the surface of the component to reflect only the properties of the metallic chromium and not the base material, the layer thickness must be at least 50 μm. However, all types of chromium plating tend to lower the fatigue limit of components [7].

2 Material and Methods

2.1 Experimental material

Stainless steel AISI 304 was used as a substrate material supplied in the form of cold drawn tubes tempered to 850 MPa. The outer diameter of the pipe 12.3 mm was then ground to a diameter of 12 ± 0.005 mm and the same roughness value max. Rz = 3 μm, inner diameter was 9.3 mm. Nominal chemical composition is in Tab. 1. Electroplated hard-chrome coatings with a thickness of min. 30 μm were applied to the outer surface of the pipe in three different industrial plants according to the specific company procedure and the experience of a particular company. However, in order to achieve a uniform layer, the tubes had to be placed during chromium plating in a preparation which rotated in an electrolytic bath for about 1 rev / min. The chromium layers were designated as A, B, and C. 3 tubes were selected from each type of chromium, which were cut to a length of 30 mm, each from the center of the tube. Subsequently, the surface microhardness was measured on them using an AFFRI Microhardness DM2D device at a load of 100 mN (Hv0.1). 10 indents were performed on each sample. The cross-sectional thickness of the chromium layer on the polished and etched samples was determined by optical microscopy.

Tab. 1 Chemical composition of AISI 304 stainless steel tube used as a substrate material

Element	Cr	Ni	Mn	Mo	Si	C	Co	P	S	Cu	V	Fe
Wt %	17.35	8.52	0.98	0.18	0.45	0.03	0.21	0.02	0.003	0.19	0.08	Re-main

2.2 Nanoindentation study

Nanoindentation tests were performed by quasistatic nanoindentation method on the device Bruker Hysitron TI-950. Quasistatic nanoindentation has become the standard technique used for nanomechanical characterization of materials. A quasistatic nanoindentation test is performed by applying and removing a load to a sample in a controlled manner with a geometrically well-defined probe. During the nanoindentation a force is applied by the transducer and the resulting displacement is observed to produce a traditional force versus displacement curve (Fig. 1). Hysitron measures the force and displacement of the nanoindentation probe with a unique patented three-plate capacitive transducer design. This transducer design provides an unsurpassed noise floor and ultra-low working force.

The nano hardness (H) was measured in the cross section of the specimen along the thickness of the chromium layer up to the substrate material. Two columns of dots with a spacing between indents of 5x15 μm were measured on each sample. The load parameters were the same for each measurement, namely the trapezoid load curve with a maximum load of 1000 μN. To obtain the hardness with negligible creep effect, experiments were carried out under the single loading and unloading cycle with a 2 second hold at the maximum load [8]. A diamond cube corner tip with an included angle of 90 ° and a radius of curvature of 40 - 100 nm was used as an induction tip.

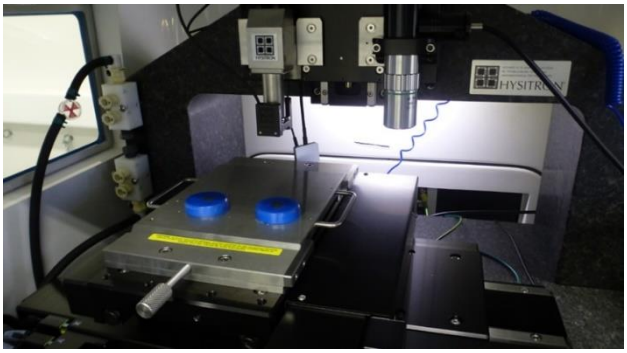

Fig. 2 Nanoindentor measuring chamber with sample locations (blue disks) [9]

3 Results and Discussion

In Fig. 3 are cross-sectional images of individual coatings, which were also used to measure their thickness. The largest thickness was in the case of coating B, where it reached values of up to 45 μm. The quality of the surface layer is best in the case of coating A, where there are the least surface and volume cracks

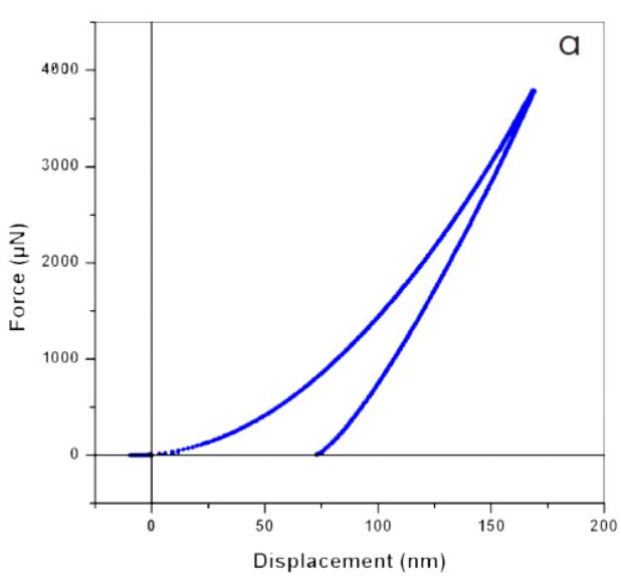

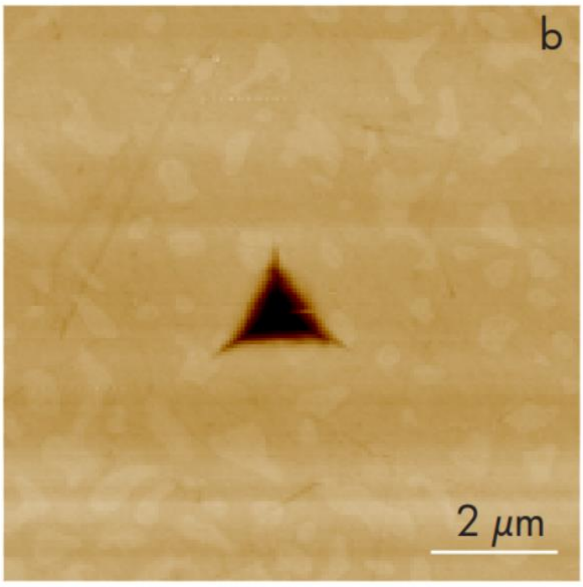

Fig. 1 a) *Typical force versus displacement curve during nanoindentation test, b) SPM image of quartz surface after quasistatic indentation showing residual indent impression*

Also the microhardness of the surface layer was the largest in the case of coating A and reached values up to 1178 Hv0.1. The lowest microhardness values were measured in the case of coating B, although this layer was the thickness, from Fig. 3 can be seen to contain the most internal pores and cracks, which can cause lower microhardness values. The microhardness of the substrate material is about 3 times smaller than the hardness of the chromium layers. All results of layer thickness and microhardness of individual layers and base material are given in Table 2. The position of the individual nanoindentation indent for each coating is shown in Fig. 4. On each coating, 21 indents were created in two columns with a gap between the columns of 15 μm and between the rows of 5 μm. The smoother chrome layer is always in the picture on the top, the base material on the bottom. Nanoindentation hardness of individual points was determined from load-displacement curves as [8, 10]:

$$H = \frac{P}{A_C} \tag{1}$$

where H is nanohardness, P is maximum load and AC is contact area [11, 12, 13]. The course of nanohardness after the thickness of individual coatings is shown in Fig. 5. Coating A shows the highest nanohardness, as was the case with microhardness. For coatings B and C, the course and values of nanohardness are similar, but in contrast to microhardness, where coating B was especially soft, it is harder in individual layers than coating C. All samples show a slight strengthening of the layer along its thickness. This was followed by a jump, which represents the difference in nanohardness between the chromium layer and the base material. In all cases, it had almost the same value, which was of course expected. From these results, it can be also seen that coating B is thicker than the other two layers.

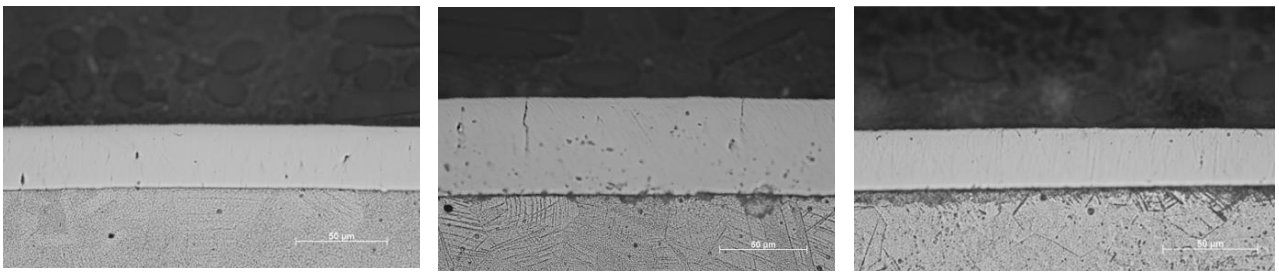

a) *b)* *c)*

Fig. 3 Cross-section of (a) coating A, (b) coating B, (c) coating C

Tab. 2 Specimens coating thickness and roughness

Coating	Coating thickness [μm]	Microhardness [$Hv_{0,1}$]
A	34.56 ± 5.12	1178.49 ± 244.40
B	45.12 ± 12.98	933.86 ± 89.70
C	32.67 ± 7.55	965.27 ± 118.16
Substrate	-	319.91 ± 169.44

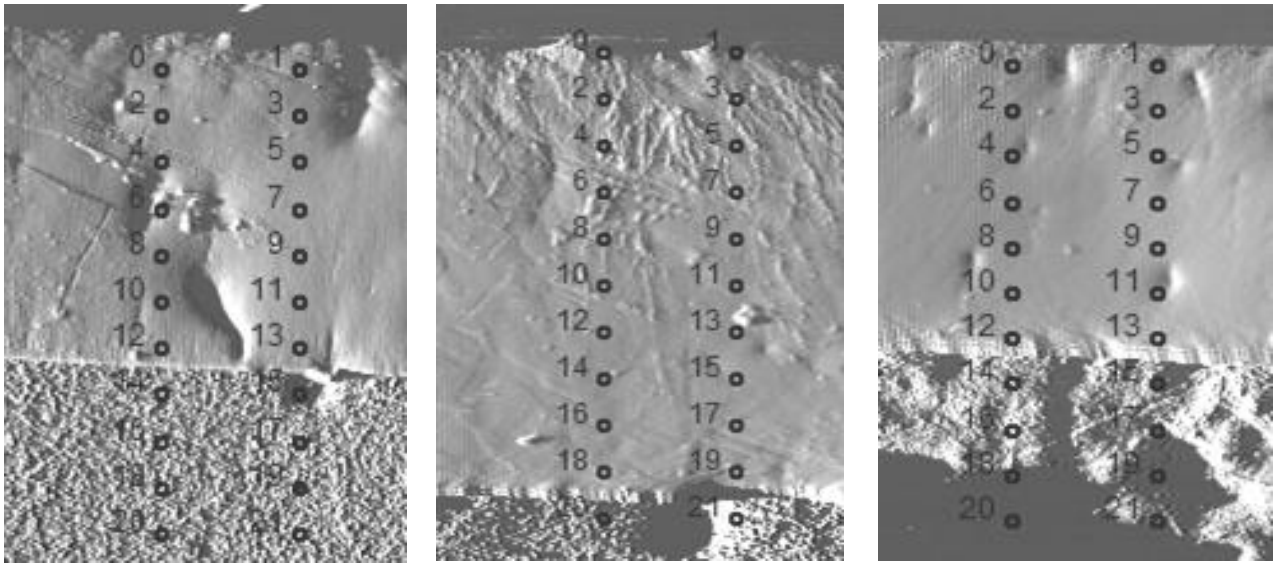

a) *b)* *c)*

Fig. 4 Position of individual indents in the thickness of the chromium layer, a) coating A, b) coating B, c) coating C

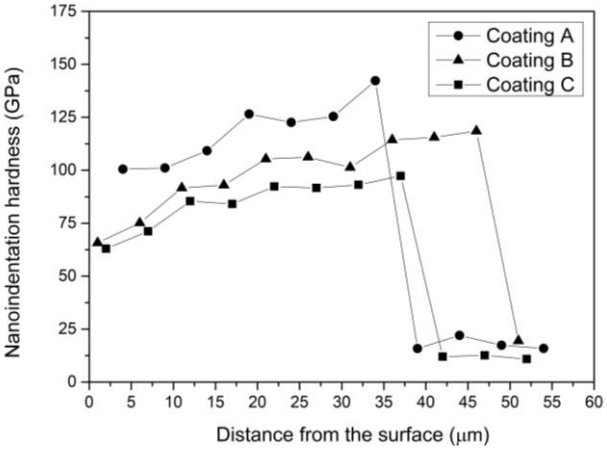

Fig. 5 Nanoindentation hardness of coatings through the thickness of coatings

4 Conclusion

This work was focused on determining the micro and nano hardness of different chromium layers on the same base materials AISI 304. From the results of microhardness it can be stated that the chromium layer increased the surface hardness by more than 3 times. In the case of the microhardness measured at the surface of the layer, it can be concluded that the thickness of the chromium layer did not affect the hardness, since the smallest hardness value was measured at the thickest layer, on the contrary

Measurement of the nanoindentation hardness over the layer thickness showed that it reflected to some extent the results of the surface hardness, and in the case of the chromium layer A layer the two highest hardnesses were achieved. Furthermore, it was found that the hardness of the chromium layer decreases with increasing thickness and is greatest at the surface of the base material.

Acknowledgement

This work was also supported by the Research Agency of the Ministry of Education, Science, Research and Sport of the Slovak Republic under the contract (ITMS2014+) no. 313011W442-CEDITEK II.

References

[1] Malzbender, J., den Toonder, J.M.J., Balkenende, A.R., de With, G.: *Measuring mechanical properties of coatings: a methodology applied to nano-particle-filled sol–gel coatings on glass*. Materials Science and Engineering: R: Reports. 36 (2002), p. 691–695.

[2] Schlesinger, M. Y., Paunovic, M. *Modern Electroplating*. Hoboken, N.J.: Wiley, 2010.

[3] Plating Resources. *DuraChrome Hard Chromium Plating*. Cocoa, Florida, 2006.

[4] Peciar, M., Fekete, R., Peciar, P.: *Agglomeration technologies of processing powder wastes*. In Solid State Phenomena. 244 (2016), p. 121-129.

[5] Fekete, R., Peciar, M., Peciar, P.: *Axiálny extrudér s rotujúcou hlavou (Axial extruder with*

rotatable die head): patentový spis 5014-2014. ÚPV SR 2015. PCT/IB2015/052668, WO2015159198A1.

[6] Peciar, P., Macho, O., Fekete, R., Peciar, M.: *Multifunkčný granulátor (Multifunctional granulator):* patentový spis 5047-2015. ÚPV SR 2017, PCT/IB2016/057081, WO2017089976A1.

[7] Lausmann, G. A.: *Current Industrial Practices Electrolytically Deposited Hardchrome*. Surf. Coating Technol., 86 (1996), p. 814-820.

[8] Oliver, W.C., Pharr, G.M.: *An improved technique for determining hardness and elastic-modulus using load and displacement sensing indentation experiments*. J. Mater. Res., 7 (1992), p. 1564-1583.

[9] Majerík, J., Barényi, Sedlák, J., Kusenda, R., Eckert, M.: *Microstructural analysis of examined 33NiCrMoV15 steel and investigation of its nanomechanical properties after machining*. Manufacturing Technology, 20 (2020), p. 72-77.

[10] Pharr, G.M., Bolshakov, A.: *Understanding nanoindentation unloading curves*. J. Mater. Res., 17 (2002), p. 2660-2671.

[11] Zeng, Z., Wang, L., Chen, L., Zhang, J.: *The Correlation between the Hardness and Tribological Behaviour of Electroplated Chromium Coating Sliding Against Ceramic and Steel Counterparts*. Surf. Coating Technol., 201 (2006), p. 2282-2288.

[12] Podgornik, B., Massler, O., Kafexhiu, F., Sedlacek, M.: *Crack Density and Tribological Performance of hard-chrome coatings*. Tribology International, 121 (2018), p. 333-340.

[13] Chen, S.: *The Coating Layer Structure of Commercial Chrome Plates*. Jour. of Electron Spectros. and Related Phen., 202 (2015), p. 1-6.

University Review, Vol. 15, Issue 4, p. 7-10, 2021.

UNIVERSITY REVIEW

MICROSTRUCTURAL ANALYSIS OF HETEROGENOUS FRICTION WELD STEEL 23B2 WITH COPPER

Matúš Gavalec[1] – Igor Barényi[2]

[1]Department of Engineering Technologies and Materials, Faculty of Special Technology, Alexander Dubček University of Trenčín, Ku kyselke 469, 911 06 Trenčín
[2] Department of Engineering Technologies and Materials, Faculty of Special Technology, Alexander Dubček University of Trenčín, Ku kyselke 469, 911 06 Trenčín

ARTICLE INFO

***Article history*:**
Received:26.11.2021
Received in revised form: 7.12.2021
Accepted:13.12 2021

Keywords:
Boron steel
Copper
Friction welding
Heterogenous weld
Microstructural analysis

Abstract:

Friction welding is effective method of joining materials, widely used not only on field of joining two different types of materials. This article is focused on friction welding of boron steel 23B2 with DHP copper. Welded workpieces were cylindrical with 10 mm diameter. Microstructural analysis was used as a control method of friction welds.

1 Introduction

Complications occur during welding of materials with different mechanical and physical properties due to different material strength during high temperature and different thermal conduction, which leads to various grade of plastic deformation. [2]

In some cases when is welded material with lower material strength with stronger material, as in the steel 23B2 and copper case, is weaker material (copper) extruded from the friction area and occurs the greater plastic deformation. Optimal conditions for weld formation of similar materials can be supervised by: machining the contact areas (various shapes), increasing the diameter of softer workpiece, preheating the stronger workpiece with external source of heat, regulation of pressure program or using support jig for softer workpiece. Some adjustments for specific materials are shown in the figure 1. These adjustments slow down deformation of the weaker material. However, these adjustments are increasing labor and metal consumption. In our case was used the manual pressure system regulation during the friction welding. [1]

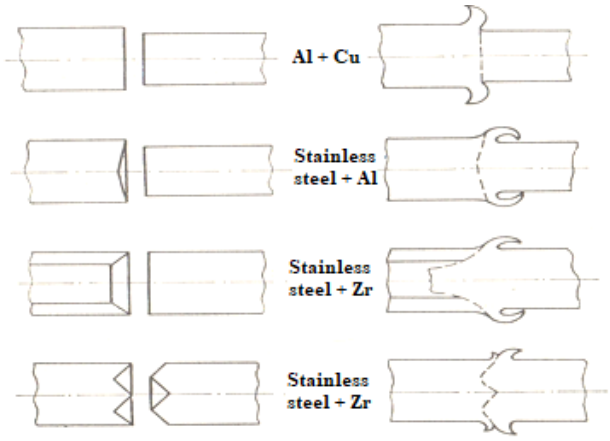

Figure 1 Some adjustments of welding workpieces to ensure uniform plastic deformation

2 Experimental details

2.1 Welding device information

Welds were made on SV 18 RA lathe (TOS Trenčín), which was not in any special way for friction welding purpose modified. As a locking element of non-rotating workpiece was used jig, which was fixed in tail stock of lathe and pressure of the workpieces ensures ejection of tail stock spindle.

2.2 Boron steel 23B2

Steel which was used during the experiments was boron steel marked as EN 23B2 (Number 1.5508), chemical composition and mechanical properties are shown in tables 1 and 2. In general contain boron steels 0,1 – 0,3 weight percentage of carbon, which guarantees good weldability.

Table 1 Chemical composition of boron steel 23B2

Chemical composition (%)							
C	Si	Mn	P	S	Cr	Cu	B
0,2 - 0,25	max 0,3	0,6 - 0,9	max 0,025	max 0,025	max 0,3	max 0,25	0,0008 - 0,005

Table 2 Mechanical properties of boron steel 23B2

Mechanical properties	
Rm (MPa)	$Rp_{0,2}$ (MPa)
625	505

2.3 Copper Cu-DHP

Copper which was used during the experiments is marked as Cu-DHP, chemical composition and mechanical properties are shown in table 3. Cu-DHP has excellent weldability properties and also is cold and hot malleable. Cu-DHP is oxidation and hydrogen cracking resistant. [4]

Table 3 Mechanical properties of boron steel 23B2

Chemical composition (%)		Mechanical properties	
Cu	P	Rm (MPa)	$Rp_{0,2}$ (MPa)
99,9	0,015 - 0,040	240 - 300	Min. 140

2.4 About the experiment

For the first bymaterial was choose copper, because copper has attractive characteristics for different requirements, which depends on mechanical properties and at the same time high formability. The main advantages of copper are high thermal conductivity, high elasticity and oxidation resistance. It is widely used in electrical and mechanical components. Welding materials based on copper is not simple, because high input heat is from joint dissipated in short time. Besides that, solders between copper and other materials like aluminum or titan have weak mechanical properties because of interlayer which contains IMC (Intermetallic Compound), this problem does not occur in friction welds.

To demonstrate the functionality of the technology was made 2 heterogenous welds steel 23B2 with copper. In figure number 2 is specimen without modification after friction welding process. On the both specimens were machined outgrowth by lathe and subsequently abbreviated to length 20 – 25 mm (fig. 3). Specimens prepared in this way was cut lengthwise, etched and thus ready for microstructural analysis, which realized on the basic on images made by optical microscope NEOPHOT 32 and evaluation software Axio vision from Zeiss company.

Problem occurred before microstructural analysis because of etching heterogenous weld since they are two different materials. Copper requires stronger etchant or longer time of etching as steel, so there is not so visible grain beside steel. If we were to etch joint longer or with stronger etchant, copper would etch better but in the case of steel it would occur overetching and blacked. [1]

Figure 2 Heterogenous friction weld steel 23B2 - copper, specimen without modification [1]

Figure 3 Heterogenous friction weld steel 23B2 - copper, modified specimen [1]

Heterogenous welds was realized by 710 revolutions per minute. Rotation speed was chosen on the basis of previous experience with homogenous friction welds of 23B2 steel.

3 Results and discussion

Microstructure from the weld area clearly demonstrates the grain refinement in weld area and graduated transition of grain thickness, in the following direction weld → weld affected zone → basic material.

We further evaluated, during welding two mechanism of materials mixture was occurred, which created good conditions for the formation of the joint – weld.

The first mechanism concerns about plastic deformation during the heat and thus a combination of heat, pressure and centrifugal force. This materials mixture are clearly visible capillary and cracking regions, indicated in figure 4.

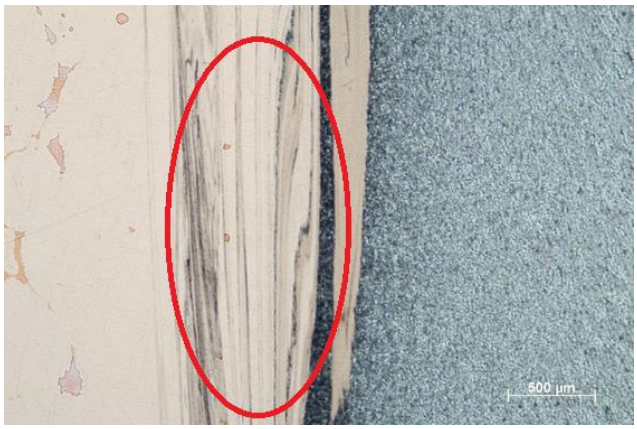

Figure 4 Microstructure of heterogenous friction weld and the area around the weld steel 23B2 – copper [1]

The second mechanism of materials mixture we attributed to diffusion of steel in copper (figure 5,6). During friction welding a group mechanism of diffusion is applied on the one hand, which is characterized as a coordinated particle motion. And other individual mechanism of diffusion, which means motion of interstitials and vacancies, which can in the welding area increase some mechanical properties, comparted to the base material. Interstitial atoms (similarly vacancies) which are smaller than ferrite atoms, they can diffuse through free spaces in the crystal lattice of the material. There are known cases, where elements from hydrogen to oxygen have diffused in iron alloys. This argumentation confirms the theory, which stated that, no alloy is leached from the weld zone during friction welding, because elements such as nickel have higher atomic weight as the ferrite, that means they have worse conditions for movement such as elements with the lower atomic weight.

I tis necessary to add, with the alloy elements, such as chrome – which has similar atomic weight as the ferrite, energy required for diffusion will become even greater, than with elements such as hydrogen, oxygen or carbon (where their diffusion from the material is desired and request relatively little activation energy), so they will diffuse to a very limited extent. Mechanism of vacancy diffusion requires more activation energy than interstitial. [1]

Figure 5 Microstructure of heterogenous friction weld steel 23B2 – copper [1]

Figure 6 Microstructure detail of heterogenous friction weld steel 23B2 – copper [1]

For the already mentioned diffusion mechanism are during the friction welding process are created ideal conditions, because of the diffusion rate in crystalline materials also increasing with increasing temperature. Another input parameter is centrifugal force which acting on atoms, alternatively groups of atoms. Centrifugal force is created by rotation of the

workpiece during the friction welding and also accelerates the individual diffusion mechanism.
Heat generation is mainly affected by selected material and the involved factors – acting axial pressure, quality of contact surfaces, friction coefficient, rpm, time, etc.

But the important thing is, whether creating welds from the same or different materials, set optimal parameters, which are suitable for selected material. Each material has different properties that need to be considered in process.

Before the friction welding is also necessary to predict the best geometry of the welded surfaces of the individual workpieces. The reason is to ensure the best possible connection of materials. This is obstacle of friction welding materials with various mechanical properties. In our case (23B2 + Cu-DHP), geometry of the contact surface has not been modified in some special way, because steel and copper which were used do not have such different mechanical and thermal properties. Especially from mechanical

- Strength
- Plasticity
- Toughness

and thermal properties

- Melting point
- Thermal conductivity
- Thermal expansion

of materials it is possible to predict the correct geometry of welded workpieces. Here I see the mentioned obstacle, because in production, it is easier to ignore the geometry of the welded surfaces, simply said – welding as it comes. This is also possible with most welded materials however, when are welded materials with very different mentioned properties, a certain preparation of the workpiece is necessary, namely in the introduction mentioned modification of the welded surfaces.

4 Conclusion

We described the theory of weld formation in rotary friction welding from available data and on the basis of physical principles before the start of experiments. From the obtained data it is possible to state that the theory has so far succeeded. Many experiments are prepared with different materials, geometries and using catalysts which confirm, supplement or refute the information described in this article.

By studying the microstructure of friction welding joints, it is possible to better understand homogenous, heterogenous welds or multimaterials structures and actually overall structural interconnection of different materials, while maintaining the condition of quality joint.

Process of the weld formation, especially the weld between two different materials, is very complex and there is a wide possibility to adjust the parameters of the machine or workpiece geometry, alternatively use of the catalysts, to obtain quality results.

5 Acknowledgement

References

[1] GAVALEC M. 2021. *Vplyv parametrov zvárania ocele 23B2 na kvalitu zvaru* : Diplomová práca, Trenčianska univerzita Alexandra Dubčeka v Trenčíne, Fakulta špeciálnej techniky Trenčín 2019, EČ: 1d2d8832-28d3-4a87-b5d1-49ad1141fd52

[2] Saini Vijay. 2014. *Friction welding – A review*, Lap Lambert Academic Publishing GmbH & Company KG, 2014, 64 s.

[3] PLÍVA, L., KAHOUN, J. 1973. *Svařování třením v praxi*. 1. vydanie. Praha: SNTL – Nakladatelství technické literatury, 1973. 7-108 s.

[4] https://www.egmgroup.it/en/product/cu-dhp/

University Review, Vol. 15, Issue 4, 11-15, 2021

UNIVERSITY REVIEW

UNNAMED VEHICLES, CONSTRUCTION AND THEIR USAGE

Pavol Mikuš

Department of Design and Special Technology, Faculty of Special Technology, Alexander Dubcek University of Trencin, Ku kyselke 469, 911 06 Trenčín

ARTICLE INFO

***Article history*:**
Received: 26.11. 2021
Received in revised form: 7.12. 2021
Accepted: 13.12. 2021

Keywords:
UAV
Carbon
Fiberglass
3D print

Abstract:

This article deals with construction of drones and materials for manufacturing of them. In next part is focused on possibilities of their usage in thermo diagnosis. This deals about technical aspects, law and from that resulted terminology, restrictions for operation and necessary permissions. In consideration of growing availability of UAV, technical and software equipment we could expect that we are on the beginning of new trend – deployment of UAV in field of technical diagnosis.

1 Introduction

Nevertheless, the field of unnamed systems is still quite young and his commercial deployment is on the market since 2015, these systems are more and more established in field of technical diagnosis.

Body, chassis, hood, cover, each people name this with another word, but it's still the same. This is the part which is on the drone the most visible. This part has very high influence on properties and useful value. This is the topic which is good to know before purchase of vehicle or by maintenance or reconstruction.

With suitable sensors are these systems used for inspections in large and hard accessible technological and another units. Today usual available sensors for UAV are RGP, LWIR and MWIR thermo cameras. The exception aren't SWIR or multispectral systems. By deployment is not only using in non-accessible objects. Using of thermo cameras in connection with UAV brings to field technical diagnosis especially overview which is for a lot of diagnosis systems very important.

Decentralized or centralized systems for thermal supply include interconnected thermal sources, thermal structures and consumer devices. Under this we could imagine heating and supply of heated water for houses and industry companies.
Flying inspection of components has two major advantages: components above the ground are often located in hard accessible terrain and for localization of components which are located under the ground (in case for localization of medium leakage from these components) is very important overview from aerial images. The thermal changes could be very small to be able to observe them from the ground. This situation is shown in the picture n.1, where we can see leakage of hot water from underground pipeline. Thermal changes on the surface with the dimensions are much bigger than men (see red circle) and this failure isn't possible to detect from the ground.[1], [2]

1.1 Construction of multicopters

In comparison with planes with hard wing isn't needed to have aerodynamic surface for the chassis of multicopters. Basically, it's very simple construction which the main task is hold the all the stuff. That means electronics, engines, camera and next equipment during the whole flight, in the best scenario during critical situation as well. Just this last-mentioned requirement shows that construction of chassis for drone requires a bit of knowledge and thinking. So basically, with enough power isn't problem to fly with almost everything, but only with good construction is possible to land and start again. In such case is possible to use this drone for useful tasks as well.[3]

1.2 The shape – advantages and shortages of solutions

The base selection of copters comes from number of engines, respective from propeller. Their number is the most often from three to eight (threecopter, quadrocopter, hexacopter or octocopter). Quadrocopters are the most common solution. For imaginations of functionality is good example as well. For another types it's not such easy to understand their functionality.

Overwhelming major of sale quadrocopters have chassis like a cross, where in the arms are usually build in drivers and on the end are engines. Electronics, batteries and next equipment are in the middle of chassis, basically in the middle of the cross. This is look of for example DJI Phantom.

The biggest advantage of this solution is simple and save of the weight. But for sure this solution has shortages as well. It's mainly relative easy damage of long arms by shock. Broken or cracked arm is the most often reason of failed landing or crash. Due to such crash could be damaged driver and engine as well. In case of one block is basically whole vehicle for scrap.

Chassis of commercial drones are in the most cases pressed from plastic – nevertheless of statement that plastic is fragile. Before construction requirements are here commercial view – serial production with huge amount and cheap material. Especially for cheaper vehicles is valid that their durability and endurance isn't on high level. Expensive solutions therefore using another materials, mainly light alloy, carbon or different sandwich construction. In the last days we can see using of 3D print. Information about materials are interesting for people which would like to build their own construction, or for people which would like to use old electronics and another stuff from old or crashed drone to the new one.

Carbon
Material which is in construction praxis and sculpture named carbon, is basically composite of carbon fibers and mineral resin. This material is extremely light and strong, due to this fact is used in flying or cosmic industry, in sport cars etc. This material has the shortage as well: expensive, fragile, strong only in few directions. His usage requires technical knowledge. Beside this manufacturing require special devices and procedures. In sculpture markets is possible to buy carbon boards, pipes and profiles. Is good to know that work with this material is risky from health point of view and this material shielding of electromagnetic field. So we have to keep in mind this fact during proposal of antennas for communication.
This material is retailed for race copters, where every single saved gram good or for big professional copters. For rest of copter's portfolio isn't relevant due to more shortages.

Fiberglass
The same as in case of carbon, the fiberglass is composite. In this material is instead of carbon fibers glass fibers. Resin could be more expensive – epoxide resin or cheaper polyester resin. Fiberglass has little bit higher weight than carbon but is still lighter and stronger than another material. To this fiberglass offer next advantages: is resistant against adverse conditions, relative cheap and easily available. In simple conditions is possible to make almost any shapes. In case of good molds is possible very easy produce spare parts.

3D print
The possibility to propose complete chassis or single parts on computer and then "print" it with simple push of button is very seductive. The same is about production of damaged parts. This option is realistic only in case, if you have access to such 3D printer and knowledge about this process. Moreover, materials which are available for 3D printers today have no such good properties like alloys of aluminum or composite materials. This shortage of 3D print is solved with bigger thickness or complicated profiles. Again, is necessary to have knowledge from mechanical engineering, Of course 3D print is very perspective technology and is good to follow this technology.[5], [6], [7], [8]

2 Technical spects of aerial thermal diagnosis

The field of aerial thermal diagnosis brings few specifics and technical restrictions.
The first restriction is that no every single UAV is able to carry thermo camera. For example the most popular model in this category DJI Phantom has not enough carrying capacity and due to this fact isn't suitable for thermo camera. So is needed choose bigger vehicles with higher carrying capacity and with option of using tilting mechanism (gimbal). Flying time of such

vehicles is about 20 – 35 minutes, it depends on weight of thermo camera, conditions of battery, weather conditions, etc. For large aerial works is necessary to calculate with higher amount of batteries, which are important alternate and in case to charge.

Second restriction is about thermo camera. Thermo camera is good known device, which is very often used for maintenance and operation of industry companies. Usually are used hand cameras, which are used in case of preventive check or prediction maintenance or static systems used like the sensors for quality system and check of assembly line or for example in research applications.

In field of aerial thermal diagnosis is necessary to calculate with fact that in present days (by comparison with wide offer hand or stationary devices) is quite limited offer of thermo cameras which are compatible with some commercial UAVs and with software for postprocessing of aerial data.

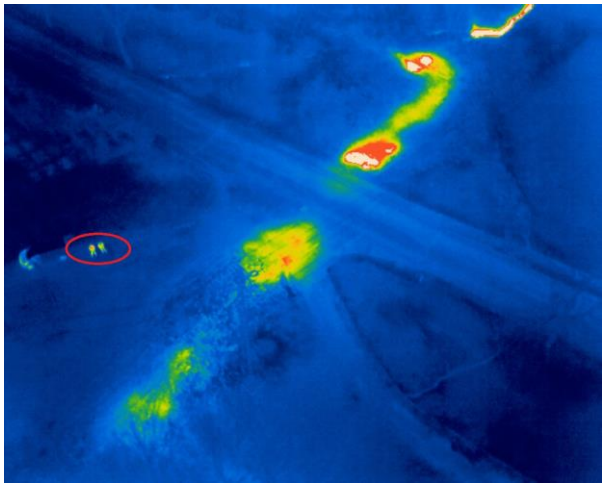

Fig. 1 The leakage of warm water from underground pipe line

Although these are classic thermo cameras with micro bolometric sensors, in case of usage with UAV they have to have communication interface due to remote control through the interface of UAV (bus PWM, S-BUS, CAN). These cameras have to be able store pictures with GPS coordinates as well. In ideal case it could be possible to control this camera with the same remote control. Unless is thermo camera equipped with corresponding communication bus, is possible shooting according GPS coordinates, altitude, etc. Good functionality is start of recording of radiometric video and automatic transfer of images according GPS coordinates. With this functionality is possible automatic choose of pictures from radiometric video according fly trajectory with defined distance. Of course, there is possible to setup single parameters and next functionalities during fly.

For illustration of technical devices, you can see on the Fig. 2 an example UAV DJI M600 with thermo camera Workswell WIRIS with resolution 640 x 512 px, lens 13 mm a thermal sensitivity 30mK.

3 Inspection of parts of heat supply systems

In case of inspection heat supply systems, we are focusing mainly on parts which could be located under or above the ground. In this application is using of thermo diagnosis matter of course. The steam or water with high temperature are carried by single components of heat supply system. Medium is insulated from external environment because of waste of heat and pressure. Damages on insulation have impact on the surface temperature and there are exist thermal bridges. Due to this fact we have quite huge thermal losses. On the picture n. 3 is possible to see higher amount of thermal bridges on the pipelines. Similar observations are quite often mainly on the older systems and this is caused by degradation of thermal insulation or not good finalization during the building.

UAV is possible to use very effective for localization parts of thermal supply system which are located under the ground. Is surprising that good insulated parts are visible by aerial checking as well. For this aerial checking have to be fulfilled few requirements: low temperature of air and ground and absence of sunshine. Such situation is possible to see on picture n. 4. Here was localization successful. In case of underground pipelines is aerial checking in comparison with hand thermo camera much more successful. Thermal changes are evaluated from higher perspective and this is not possible to do from the ground.[4]

The right question is maximal depth of installation of systems when is possible to sense thermal leakage. Answer on this question is not simply because it depends on amount of leak water, temperature of medium, temperature of the ground, influence of sun, etc. Common installation depth is 1 – 2 meters.

Fig. 2 UAV DJI M600 with thermo camera Workswell WIRIS

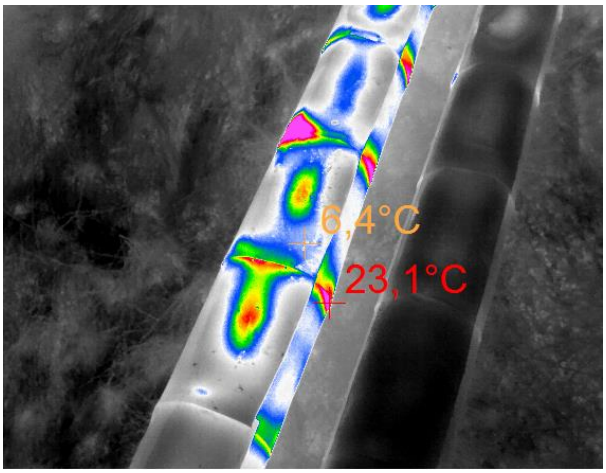

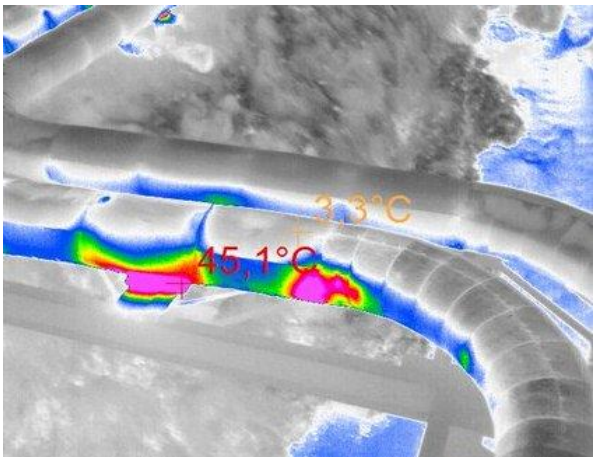

Fig. 3 Thermal bridges on thermal pipe lines

4 The law about unnamed aerial vehicles

This article wouldn't be complete unless we are not mentioned the law and few restrictions which are results of this law. Supervision for operation, certification of UAVs and pilot's licenses in Slovak Republic performs Civil Aviation Authority. Operations of UAV is in category civil aerial operation and therefore we have to keep valid legislative rules. According to law the flights are possible to carry out only for distance of direct visual contact with UAV (without any additional equipment it's about 200 – 500m). This rule is due to correct evaluation of situation around the UAV – some obstacles, etc. The flight with AUV could be carried out only in case of no damages on human health, property, environment and safe of flight. The flight with UAV isn't possible to everywhere. In general, the flights aren't possible to do above dense occupied areas, above persons without their approval, above roads and trails or in near of airport. Only Civil Aviation Authority could make an exception from mentioned rules.

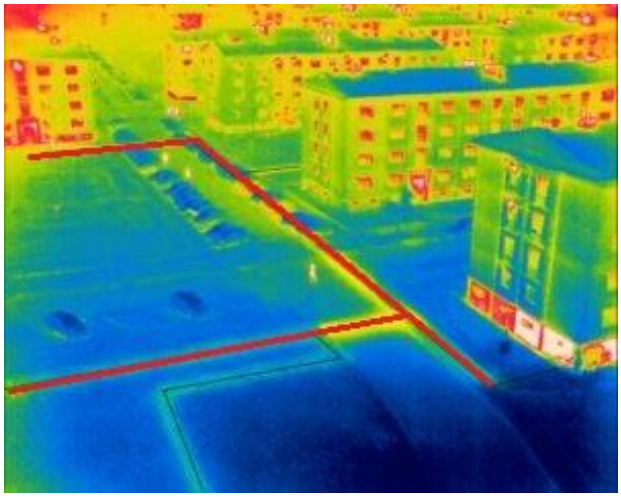

Fig. 4 Localization of underground pipelines with aerial thermo diagnosis

The flight of plane could be carried out with two options: like a service for payment or aerial activity for your own need. In both cases in necessary to have permission from Civil Aviation Authority. For this you have to make theoretical and practical exams.

5 Conclusion

In the face of law and technical restrictions is aerial thermo diagnosis field with good perspective, in field of technical inspection of thermal supply systems as well. Deployment of this technique isn't only about measurement in hard accessible places, this brings to the field of technical diagnosis mainly the overview, which is in the lot of situation very

needed. In consideration of growing availability of UAV, technical and software equipment we could expect that we are on the beginning of new trend – deployment of UAV in field of technical diagnosis.

References

[1] **Swiatkowski, K., Hatalak, R.:** *Study of the new floating-plug drawing process of thin-walled tubes, Journal of Materials Processing Technology,* **Vol. 151, 2004, No. 1-3, p. 105–114.**

[2] **Zemko, M., Kvačkaj, T.:** *Numerical simulations of production technology of rear suspension sub-frame member by hydroforming, Acta Metallurgica Slovaca,* **Vol. 4 2005, No.4, p. 412-418.**

[3] **Besterci, M.:** *Dispersion-strengthened aluminium prepared by mechanical alloying,* **1st ed., CISP, London, 1999.**

[4] **Breznická, A., Pivko, Š.:** *Využitie nových digitálnych technológií v prístupoch riadenia procesov údržby,* **In: ICMT´ 2018 : Medzinárodná vedecká konferencia o vojenských a špeciálnych technológiách. - Trenčín : TnUAD, 2018. - ISBN 978-80-8075-806-6. - s. 72-77, CD ROM.**

[5] **Kvačkaj, T.:** *Metallurgical and geometrical substance of quality development in flat rolled products,* **1st ed., Štroffek, 1999, (in Slovak).**

[6] **Martín, J. M., Navarcorena, B., Arribas, I., Gómez-Acebo, T., Castro, F.:** *Dimensional Changes and Secondary Porosity in Liquid Phase Sintered Al Alloys,* **In.: Euro PM 2004, Wien, EPMA/Shrewsbury, Vol. 4, 2004, p. 46-53.**

[7] **Mondolfo, L. F., et al.:** *Aluminium alloys, Structure and properties,* **1st ed., Butterworth, London, 1976.**

[8] **Rumlová, M., Popardovský, V.:** *Dynamic balancing of the tricopter drive unit,* In**: Armament and Technics of Armed Forces 2019, 25th International Scientific Conference, Liptovský Mikuláš, ISBN 978-80-8040-585-4, - s. 213 - 226**

University Review, Vol. 15, Issue 4, p. 16-19, 2021.

UNIVERSITY REVIEW

THE APPLICATION OF LASER HARDENING MATERIAL

Milan Jus[1]

[1]Department of Mechanical Desing and Special Technology, Faculty of Special Technology, Alexander Dubček University of Trenčín, Ku kyselke 469, 911 06 Trenčín, Slovakia, E-mail address: milan.jus@tnuni.sk

ARTICLE INFO (10 pt, bold)…filled by the publisher

***Article history*:**
Received: 26.11. 2021
Received in revised form: 7.12.2021
Accepted:13.12. 2021

Keywords:
heat treatment, laser melting, microstructure, precipitation-hardened, laser powder bed fusion

Abstract:

This article deals with the possibilities of heat treatment of the material, rather its part, to achieve the required properties, which are required in further activity. Particular attention is paid to laser treatment.

1 Introduction (12 pt, bold)

In general, a material, more precisely expressed as a component, a product of a material, can be heat treated as a whole, in its entirety, or only in certain parts, which are to have other properties.

In practice, we encounter the fact that we need to strengthen the surface part of the material in some way. We divide coating methods on the basis of the application process, which is carried out by chemical or physical means. In principle, we know the application of PVD (Physical vapor deposition) and CVD (Chemical vapor deposition).

The main technological difference between these two methods, which limits or predetermines the suitability of their use for tool material, is the temperature of the process itself. With the PVD method, we operate with a working temperature below 500 °C, which guarantees that there will be no thermal influence and subsequent structural changes in the tool material (mainly HSS steel). [1][2]

The operating temperature of the CVD method is in the range of 1000 to 1200 °C, so it is suitable for coating material that has guaranteed temperature resistance in this range. Examples are sintered carbides. The applicability of the CVD method is extended by its various modifications, such as MTCVD (Middle temperature chemical vapor deposition), which means the application of technology at reduced (medium) temperatures. [3][4]

Hardening can be a process where we have a loose material that we strengthen, cure by a certain process, so that we create a solid structure of the material. The energy supplied by which we perform the hardening can be by means of a laser beam.

Table 1 Ways of technology implementation PVD and CVD

Methods of PVD
Thermal induction
Plasma induction
Electron induction (electron beam)
Photon beam induction (e.g. laser)
Principles of CVD
Steaming
Sputtering
Ion implantation

2 Use of a laser to harden steel

Martensitic stainless steels are widely used in industry. This is mainly in view of their high strength and good corrosion resistance. Precipitation hardened martensitic stainless steels have a very high strength compared to other stainless steels. This is about 3-4 times more than austenitic stainless steels (such as 304 and 316). Due to the poor processability due to the high strength and hardness caused by precipitation hardening, it limits the extensive use of stainless steels (precipitation hardened) as structural elements of complex shapes.

Powder bed laser fusion is an additive manufacturing technology that not only offers the benefits of producing complex and precise parts with a short delivery time, but also eliminates or limits the subsequent machining process. [5]

3 Hardening equipment

The mechanism used for hardening is very similar to a 3D printer. The movement takes place in the Cartesian space, where the individual movements are realized as translational in the x-axis and y-axis. The movement in the z-axis is carried out by translationally moving the bed of material. In this case, it is possible to change the position of the print head (3D printer) by a deflection device, since a laser beam is used for hardening. But even in this case, it is preserved that we use two degrees of freedom in the mechanism of movement.
Furthermore, it is necessary to ensure the addition of material (adding material) to the bed. This requires a mechanism with one degree of freedom that will ensure translational movement in one axis.
Unlike a 3D printer with this hardening device, it is still necessary to ensure that the given working space is in a closed chamber, so that such a chamber is filled with the required gas.
A schematic of the laser powder bed fusion process is shown in Fig. 1.

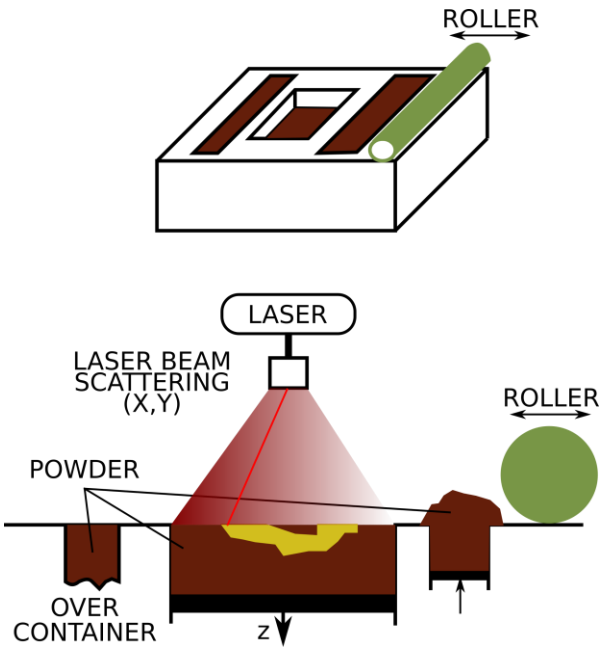

Fig. 1 Schematic of the laser powder bed fusion process

The scanning process can be different. It is necessary to optimize this process so that the created object has the best possible properties.
The basic types of laser scanning are according to the main directions. The scanning direction can be horizontal so that it takes place in one direction, it is also characterized in that it takes place in 0 degree. Another type of scanning is the previous horizontal only extended by another direction, so it is a horizontal way at 0 and 180 degrees. The other two methods of laser scanning are in the vertical direction, where the first method is at 90 degrees and the second vertical method is also in the opposite direction, so that 90 and 270 degrees are used. Another possibility of creating a pattern is the so-called a concentric pattern, which is created as an outer contour and it gradually progresses towards the inside of the object. Another pattern used is hexagonal, where the hexagons can be joined at an angle of 45 degrees to the load axis. [5][6]

A schematic illustration of possible laser scanning methods is shown in Fig. 2.

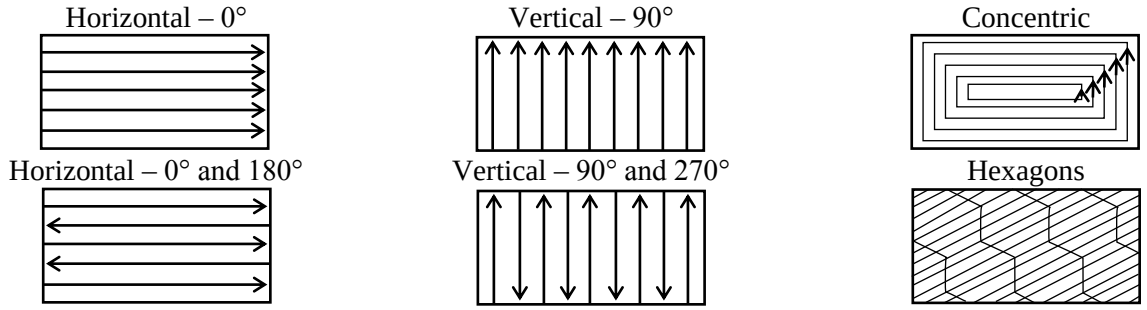

Fig. 2 A schematic illustration of possible laser scanning methods

The laser curing process is performed in a gas chamber (e.g. argon or nitrogen) to prevent possible oxidation.

The powder material used can be of various types and also modified in a certain way, which also depends on the properties of the final object which we produce in this way. During the hardening process, various phase transitions of this material take place.

Powders can be obtained from gas atomization (atomized in argon and nitrogen) or atomized in water. Gas-atomized powders have spherical particles, while water-atomized powders have a mixture of hemispherical and rounded shapes with relatively pure particles without satellites. The atmosphere of the building (argon or nitrogen) is necessary to prevent oxidation of the powder during the hardening process at elevated temperature. [5][7]

The effect of different atomizations of the medium on the microstructure of the powder is huge. It is made by a nitrogen atomized powder, austenite is easier to obtain than an argon powder, and a water atomized powder can obtain a maximum volume fraction of austenite in three atomization modes. [5][8][12]

During the creation of the object itself, there are many influencing factors that affect the quality and mechanical properties of the final product. In addition to the already mentioned influencing factors, it is possible to consider the orientation of the object itself, as well as the used method of the scattered laser beam, which is shown in the Fig. 2. Another influencing factor is the amount of energy density used in the hardening process.

From the point of view of evaluating the hardening process itself, it is necessary to perform various measurements and tests. Mechanical and metallographic properties are evaluated. Furthermore, it is possible to evaluate the influence of process parameters on hardness. The orientation of the building, the time intervals between the layers and the energy density can influence the thermal history that occurred during production, resulting in a different retained amount of austenite in the microstructure, showing a different microhardness. The correlations between scanning speed, hatch spacing, cut thickness and microhardness have a declining trend. Volume percentage and size of Cu precipitates play an important role in changing the microhardness. [5][9]

During the transition from the original state directly to the aging heat treatment (without solution treatment), the change in hardness values depends on the amount of retained austenite, which is dictated mainly by the original atomization state of the powder. [5][10]

The amount of austenite retained can greatly depend on different production conditions. The volume percentage of retained austenite can significantly affect material strength, toughness, tensile strength, and elongation to failure. As the content of the retained austenitic phase increases, the tensile strength and hardness of the parts decrease, while the retained austenite is beneficial in improving hardening and elongation at break due to the effect of transformation-induced plasticity (TRIP). [11]

If we consider the orientation of the samples, then compared to the horizontal, the vertical sample has a small volume per unit volume and a large porosity. In the case of a vertical sample, the weak interfacial layer is perpendicular to the direction of the tensile load, provided there is an easier path for the pores to grow and merge. However, in horizontal samples, these layers are parallel to the load axis, which prevents the opening and widening of the cavities. [5]

The increase in strength can be attributed to the relatively higher density of the part produced at the higher density of laser energy, which produces sufficient heat to melt the powder, and the fraction of the martensitic phase increased in the part made of water-atomized powder. The hardening effect is attributed to the heat treatment on the strength (yield strength and tensile strength) of the second phase precipitate in the matrix, as well as other changes in the characteristics of the microstructure, phase volume fraction (relative volume fraction of martensite

to retained austenite), grain size and morphology. In addition, cavities, pores, and unmelted areas (i.e., weaker metallurgical bonds) between the layers can be attributed to the entrained depth of the entrained gas and the lower laser. Such cavities have a clear effect on the mechanical properties of the materials, in particular their elongation at break and fatigue properties. [5]

It is important for components to pay attention to their fatigue behavior. This is mainly because fatigue failure is the most common manifestation of failure in many engineering components and structures. Fatigue failure is the result of cyclic (repeated) loading and can occur when the stress is much less compared to the monotonic failure caused.

4 Conclusion

This article presents the material curing process. The mechanism is similar to a 3D printer, where curing is carried out by means of a laser beam, the material itself is powdered and the process takes place in a protective atmosphere. The final quality of the cured article is influenced by several factors, such as: the type of powder material used, the orientation of the cured article, the laser beam scattering method used, the amount of energy density of the curing beam used.

5 Acknowledgement

Author is grateful for the support by the Research Agency of the Ministry of Education, Science, Research and Sport of the Slovak Republic under the contract (ITMS2014+) no. 313011W442-CEDITEK II.

References

[1] Forejt, M., Píška, M.: *Teorie obrábění, tváření a nástroje*, Brno: Akademické nakladatelství CERM, 2006. ISBN 80-214-2374-9.

[2] *INCONEL Alloy718*, [02.11.2021], https://www.specialmetals.com/assets/smc/documents/alloys/inconel/inconel-alloy-718.pdf.

[3] Sugihars, T., Tanaka, H., Enomoto, T.: *Development of Novel CBN Cutting Tool for High Speed Machining of Inconel 718 Focusing on Coolant Behaviors*, Procedia Manufacturing 10, 2017, p. 436-442, [03.11.2021], DOI: 10.1016/J.PROMFG.2017.07.021. ISSN 23519789.

[4] Humár, A.: *Materiály pro řezné nástroje*, 1. Praha: MM Publishing, 2008. ISBN 978-80-254-2250-2.

[5] Zai, L., et al.: *Laser Powder Bed Fusion of Precipitation-Hardened Martensitic Stainless Steels*, Article in Metals - Open Access Metallurgy Journal, February 2020, [03.11.2021], https://DOI: 10.3390/met10020255.

[6] Kudzal, A., et al.: *Effect of scan pattern on the microstructure and mechanical properties of Powder Bed Fusion additive manufactured 17–4 stainless steel*, Mater. Des. 2017, 133, p. 205–215, [04.11.2021], http://dx.doi.org/10.1016/j.matdes.2017.07.047

[7] De Nisi, J., et al.: *Precipitation hardening stainless steel produced by powder bed fusion: influence of positioning and heat treatment*, Procedia Structural Integrity 24 (2019), p. 541–558.

[8] Rafi, H. K., et al: *Microstructure and Mechanical Behavior of 17–4 Precipitation Hardenable Steel Processed by Selective Laser Melting*, J. Mater. Eng. Perform. 2014, 23, p. 4421–4428, [04.11.2021], http://dx.doi.org/10.1007/s11665-014-1226-y.

[9] Osten, J., et al.: *Development of Precipitation Hardening Parameters for High Strength Alloy AA 7068*, Materials 2020, 13, 918; [07.11.2021], https://doi:10.3390/ma13040918.

[10] Rowolt, Ch., et al.: *Dissolution and precipitation of copper-rich phases during heating and cooling of precipitation-hardening steel X5CrNiCuNb16-4 (17-4 PH)*, Metals & corrosion, Journal Mater Sci (2020) 55, p. 13244–13257.

[11] Rowolt, C., et al.: *Quantitative high temperature calorimetry on precipitation in steel and nickel alloys*, 2019, Thermochim Acta 677: p. 169–179, [07.11.2021], https://doi.org/10.1016/j.tca.2019.01.026.

[12] Breznická, A., Chovanec, A.: *Stochastické modelovanie zložiek spoľahlivosti pomocou metódy stromu porúch*. In: Transfer 2017 : Využívanie nových poznatkov v strojárskej praxi. - Trenčianske Teplice : TnUAD FŠT, 2017. [6 s.] CD-ROM. - ISBN 978-80-8075-787-8.

University Review, Vol. 15, Issue 4, 20-25, 2021.

UNIVERSITY REVIEW

POSSIBILITIES OF DETERMINING THE FRAGMENTS SPEED AFTER DETONATION BY CALCULATION

Ľudmila Timárová

[1]Department of Mechanical Engineering, Faculty of Special Technology, Alexander Dubček University of Trenčín, Ku kyselke 469, 911 06, Trenčín

ARTICLE INFO

***Article history*: (9*pt, bold italic*)**
Received: 26.11. 2021
Received in revised form: 7.12. 2021
Accepted: 13.12. 2021

Keywords:
Take of speed
Fragments
Explosive

Abstract:

The article describes methods for determining the speeds of fragments, which arise from the division of the body of the projectile or the payload by detonation of the working charge. The article summarizes the calculation methods for individual types of shells and charges. At the end of the article, the calculation of speed of the fragments, which arises during the shattering of the steel body of a 20 mm caliber projectile using a TNT filling, is given. The article also describes ways to verify the calculated values.

1 Introduction

At present, the demand for new types of ammunition, the task of which is to destroy special targets, is gaining ground in advanced armies. Increasing attention is being paid to the elimination of armored vehicles. On the other side, there is ammunition, the effect of which in the target should be such that it allows the elimination of only the target and does not cause unnecessary material damage. This type of ammunition can include, for example, "payloads" of unmanned aerial vehicles. These types of loads are transported to the place of use either by a kamikaze UAV means or by a means capable of providing repeated transport.

On the modern battlefield, UAVs in the field of observation have become an indispensable part in the conduct of modern combat. They provide a realistic picture of the situation on the battlefield and thus allow operational decisions to be made to eliminate potential dangers and minimize losses.

In real conditions, we encounter terrorism, which uses available conventional manufactured aircraft on which conventionally produced ammunition is placed - e.g. 40 mm grenades, which are adjusted with plastic tubes and badminton baskets, which provide stabilization when falling on target.

Fig. 1 Conventopnal UAV with improvised ammunition

Fig. 2 Detail view on improvised ammunition

In this paper, we will deal with the acceleration of metals by the detonation of explosives. This process is widely used in military as well as civilian practice. In military practice, it is most often used to determine the take-off speed of fragments, which arise after the initiation of an explosive charge placed in the projectile. These theoretical calculations will provide information on what take-off speed can be achieved and thus ensure the required kinetic energy of the shard, which has the task of disabling not only the technology but also the manpower of the enemy.

During fragmentation process, projectiles should have large number of fragments to increase probability of hit on target.

Fragments density enabling multiple hit on a target with enough kinetic energy for target penetration. Lethal fragment range depends on initial velocity, fragment ejection angle, mass and shape of fragment.

Projectiles with natural fragmentation technology are characterized by low cost of manufacturing, wasted mass/energy, and least mass efficient at target.

Embossed fragmentation projectiles or ammunition technology is characterized by less wasted mass/energy, improved lethality, and low cost of manufacturing. This kind of technology is not applicable in artillery projectiles since there is high axial acceleration during the launching phase and this could jeopardize structural strength of
the projectile body. This kind of fragmentation has been in use for a long time with guided and unguided rocket warheads. Inside of the warhead there are integrated segments which have partially formed fragments.

Preformed fragmentation projectiles or warheads technology characterizes efficient mass/energy, optimized lethality and more cost of manufacturing and most mass coefficient. Modern artillery projectiles with preformed fragments are usually equipped with large amount of pre formed fragments which are formed as a sphere or a cube made of steel or tungsten and positioned in front and in
the middle of projectile built in cured polymer matrix.

2 Take-off speed calculation models

When calculating the take-off speed, we assume that the take-off speed has the same value for all weight categories of shrapnel. Fully formed shrapnels have a 10 to 25% lower take-off speed than shrapnel made randomly from a homogeneous grenade body. Special type is projectile body with pre fragmetation. When calculating the take-off speed, we often encounter a filling coefficient - Kω, which indicates the ratio between the weight of the used explosive and the total weight of the grenade without the initiation device.

Fig. 3 Projectile with homogenous body

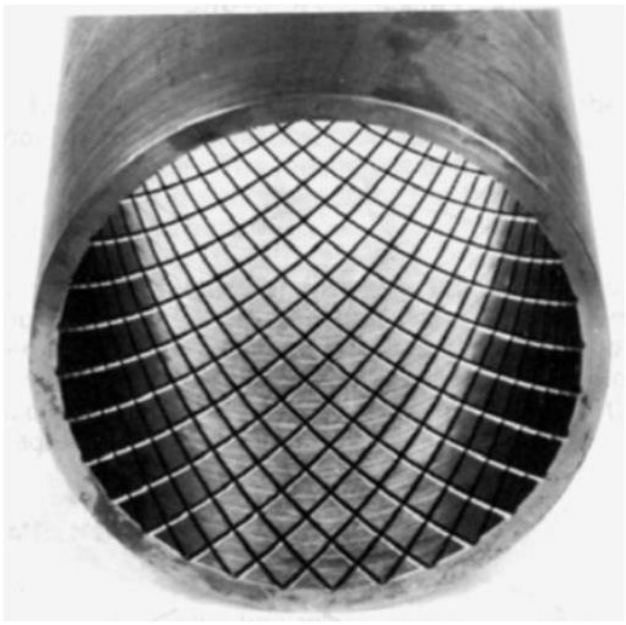

Fig. 4 Steel body with pre formed fragments

Fig. 5 Matrix with fully formed shrapnels

2.1 Formulas for determining the take-off speed of shards without the author

In the literature, we can find formulas that provide quick and easy information about the take-off speed of shards. The following formulas can be included among such formulas [5].

$$v_r = (0{,}75 \div 0{,}90) \cdot v_d \cdot \frac{m_\omega}{m_0} \quad (1)$$

$$v_r = \frac{v_d}{2} \cdot \sqrt{\frac{0{,}9 \cdot m_\omega}{2 \cdot m_0 + m_\omega}} \quad (2)$$

$$v_r = \frac{v_d}{2} \cdot \sqrt{\frac{K_2 \cdot m_\omega}{2 \cdot m_0 + m_\omega}} \quad (3)$$

v_d – detonation velocity of the explosive [m.s^{-1}],
m_ω – explosive mass [kg],
m_c – total projectile weight [kg] $m_c=m_0+m_\omega$,
m_0 – projectile body weight [kg].

Tab. 1 Coefficient K_2

explosive	m_ω/m_c					
	0,10	0,11	0,12	0,13	0,14	0,15
TNT	0,81	0,82	0,82	0,83	0,84	0,84
TNT/HMX	0,76	0,77	0,77	0,78	0,79	0,79

2.2 Gueney's model for determining the take-off speed

During World War II, American physicist R.W. Gurney designed and implemented a simple model based on which he derived the speed of explosion-accelerated shards. The calculation model was based on two assumptions:

a) Detonation of a given explosive releases a certain amount of energy per unit mass of the explosive and this energy is distributed to accelerate the inert material - in the form of kinetic energy and to the energy transferred by the gaseous product of combustion.

b) These gaseous products have a spatially uniform density and a linear 1D velocity profile in the spatial dimensions of the system.

Primarily, the energy that is of the total energy usable for accelerating inert matter, expressed in terms of velocity (km.s^{-1}), is characteristic of each type of explosive and its specific density. It is called $(2E)^{1/2}$ – Gurney's speed. The exact determination of this speed is performed experimentally [3, 4].

Gurney's formula I.

$$v_{r(i)} = \sqrt{2 \cdot E} \sqrt{\frac{G_{(i)}}{1 + 0{,}5 \cdot G_{(i)}}} \quad (4)$$

$$G_{(i)} = R \cdot F_{(i)} \cdot \frac{m_\omega(i)}{m_{(t)}(i)} \quad (5)$$

i - i-th section - distance from the front of the filling (place of initiation),

$\sqrt{2 * E}$ – explosive characteristics,

R – a constant expressing the influence of the design. Preformed shrapnel R = 0.75, random decomposition R = 1.00,

F(i) – correction function depending on the shape of the filling and the place of initiation.

Tab. 2 Characteristic parameters of explosives

Explosives	Explosive density [kg.m^{-3}]	Detonation speed [m.s^{-1}]	$\sqrt{2*E}$ [m.s^{-1}]
TNT	1630	6940	2370
Pentrit	1760	8260	2930
Hexogen	1770	8640	2830
Octogen	1890	9110	2970

Gurney's formula II.

It allows you to determine the take-off speed with respect to different body thickness of the grenade wall or. different diameter of explosive in a given section. The formula is suitable for calculating the flying speed of fragments formed from a long tube.

$$v_r = \frac{\sqrt{2 \cdot E}}{\left[\frac{M}{C} + \frac{1}{2}\right]^{\frac{1}{2}}} \tag{6}$$

$$\frac{M}{C} = \frac{\rho_k (D_v^2 - d_0^2)}{\rho_k \cdot D_v^2} \tag{7}$$

√(2*E) – explosive characteristics,
M/C – ballistic ratio,
ρ_k – projectile body density,
ρ_ω – explosive density,
d_0 – inner diameter of the projectile body,
D_v – outer diameter of the projectile body.

2.3 Bakar's formula

Bakar's formula uses the mechanical properties of the projectile body and the explosive constant to determine the take-off speed. This formula has the disadvantage that each explosive is assigned an explosive constant At and this must be determined experimentally [3].

$$v_r = A_t \cdot \frac{\sqrt{K_\omega}}{\sqrt[27]{R_m}} \cdot \sqrt[50]{Z} \tag{8}$$

A_t – constant according to the type of explosive (for TNT = 2736),
K_ω – filling factor,
R_m – the strength limit of the projectile body material
Z – relative narrowing (contraction) usually 0.2 to 0.5.

2.4 Pokrokov´s formula II [5]

$$v_r = 2500 \cdot \sqrt{(K_\omega - a_m)} \tag{9}$$

K_ω – filling factor,
a_m – the material constant of the projectile body, for steel it is equal to 0.05 and for steel for castings 0.02.

2.5 Gabeaud's formula for calculating the take-off speed [5]

$$v_r = 1{,}4185 \cdot \sqrt{p_m} \cdot \sqrt{\frac{1}{\rho} \cdot \left(1 - \frac{A}{100}\right) \cdot \left(1 + \frac{A \cdot d}{200 \cdot t}\right) \cdot \left(1 - \frac{200}{100 - A} \cdot \frac{t}{d}\right)} \tag{10}$$

d – projectile caliber [m],
t – wall thickness [m],
A – ductility of the projectile body material [%],
P – projectile body material density [kg.m^{-3}],
P_m – maximum pressure developed by the explosive in a closed container (for TNT = p_m=5*10^9 Pa).

2.6 Baum's formula for calculating the take-off speed

$$v_r = \frac{C_a}{4} \cdot \sqrt{\frac{v_d^2}{4} \cdot \frac{m_\omega}{2 \cdot m_0 + m_\omega}} \cdot \left[1 - \left(\frac{r_0}{r}\right)^4\right] \cdot \frac{2 \cdot R_{ED} \cdot m_\omega}{r_0^2 \cdot \rho_\omega \cdot m_0} \cdot h_0^x \cdot (2 \cdot r_{0x} + h_{0x}) \cdot \ln\left(\frac{r}{r_0}\right) \tag{11}$$

v_d – detonation velocity of the explosive [m.s^{-1}],
m_ω – explosive mass [kg],
m_c – total projectile weight [kg] $m_c=m_0+m_\omega$,
m_0 – projectile body weight [kg],
r_{0x} – inner radius of the projectile cavity in section x,
h_{0x} – wall thickness in section x ($h=-r+\sqrt{(r^2+a)}$),
r_0 – initial inner radius of the projectile cavity,
ρ_ω - explosive density,
C_α – correction function depending on the distance from the initiation point and the initiation position.

3 Example of take-off speed calculation

Determine the take-off speed of shrapnel for a 20 mm projectile with a wall thickness of 3 mm. The body of the projectile is made from steel with a density of 7800 kg.m^{-3} and an elongation of 15%. TNT is used as the explosive charge.

We used Gabeaud's formula to determine the take-off speed.

$$v_r = 1{,}4185 \cdot \sqrt{p_m} \cdot \sqrt{\frac{1}{\rho}} \cdot \left(1 - \frac{A}{100}\right) \cdot \left(1 + \frac{A \cdot d}{200 \cdot t}\right) \cdot \left(1 - \frac{200}{100 - A} \cdot \frac{t}{d}\right) = 1{,}4185 \cdot \sqrt{5 \cdot 10^9} \cdot \sqrt{\frac{1}{7800}} \cdot \left(1 - \frac{15}{100}\right) \cdot \left(1 + \frac{15 \cdot 0{,}02}{200 \cdot 0{,}003}\right) \cdot \left(1 - \frac{200}{100 - 15} \cdot \frac{0{,}003}{0{,}02}\right) = 1031{,}6 \frac{m}{s} \quad (12)$$

4 Conclusion

Needs for cost reduction of military operations at low intensity battles, which are often taking place in urban areas, have caused development of new types of projectiles with longer range, more accuracy, preciseness at target and greater lethal efficiency at the target.

Inside the lethal area of natural fragmentation projectile, fragments, all different in shape and mass, are moving mostly at the supersonic velocity. Fragments formed by natural fragmentation process have irregular shape. While flying through the space, multiple shockwaves are formed on their surface which results in sudden drag increase and rapid decrease in its velocity.
Application of natural fragmentation technologies in modern HE artillery projectiles means possession of high fragmentation steel production technology and thermal procession control of the steel,applying high performance explosives and IM characteristics. Realistically, very few developed countries have this knowledge and technologies. New trend in application of preformed fragments in modern projectiles requires even more specific knowledge and technologies, thereby reducing the number of countries capable of manufacturing modern artillery projectiles with significantly higher lethal efficiency.
In practice, we can encounter six ways to calculate the take-off speed. An appropriate methodology must be selected to calculate the take-off speed. Most calculations are based on practical experiments.
Verification of these calculations is complicated. It can be performed using a Doppler radar, which must, however, be suitably positioned to prevent it from being destroyed by flying fragments. Another method for verifying these calculations is to measure the speed using frames. At a specified distance, we set the frames, which are woven with lacquered copper wire of minimum diameter. These frames are connected to an oscilloscope capable of detecting an open circuit. After detonation, the moment of detonation becomes the start signal. When the wire breaks on the frame, a stop signal occurs. Since we know how far the frame is from the place of detonation and we know the time from the beginning of the initiation to the stop signal, we can determine the take-off speed at that distance.
These methods of verification or even determination of the take-off speed are demanding, but often required. This is one of the evaluation parameters of function and work ability when designing payloads. Knowledge of the take-off speed at pre-fragmented payloads will allow the determination of the kinetic energy of the fragments and thus the wound potential.

[1] Vávra, P. 2008. *Teorie výbušin*. Pardubice: Univerzita Pardubice, 2008. 101 s. ISBN 978-80-7395-116-0.

[2] Zeman, S. 2007. *Texty přednášek z prědmětu Technologie základních výbušin (Technologie energetických materiálu I)*. Pardubice: Univerzita Pardubice, 2007. 146 s. ISBN 987-80-7194-55-715-07.

[3] Brebera, S. 2007. *Vojenské trhaviny a technologie výroby trhavinových náloží*. Pardubice: Univerzita Pardubice, 2007. 111 s. ISBN 80-7194-725-3-55-701-05.

[4] Vávra, P. – Vágenknecht. J. 2004. *Teorie působení výbuchu*. Pardubice: Univerzita Pardubice. 2004. 105 s. ISBN 80-7194-4947-55-782-02.

[5] Kusák, J. a kol. 2008. *Základy konstrukce munice I*. Pardubice: Univerzita Pardubice. 2008. 375 s. ISBN 978-80-7395-123-8.

[6] Pivko, Š., Breznická, A. 2018. *Rámcový návrh modelu opatrení, ktoré pomôžu predvídať správanie výbušných materiálov v extrémnych klimatických podmienkach s dopadom na ich účinnosť*. In ICMT´ 2018: Medzinárodná vedecká konferencia o vojenských a špeciálnych technológiách. - Trenčín: TnUAD, 2018. - ISBN 978-80-8075-806-6. - s. 78-82, CD ROM.

[7] Zecevic, B., Terzic, J., Catovic, 2004. *A. Influence of Warhead Design on Natural Fragmentation Performances*. In Annals of DAAAM for 2004 & Proceedings of the 15th International DAAAM Symposium, Vienna 2004.

[8] Reynolds, M., Huntington-Thresher, W. 2016. *Development of tuneable effects warheads***.** In Defence Technology. Vol. 12, No. 3, p. 255-262.

[9] Zecevic, B., Terzic, J., Razic, F., Serdarevic-Kadic, S. 2015. *Lethal influence factors of natural and preformed fragmentation projectiles*. In Daaam international scientific book 2015. Chapter 20, p. 219-234.

University Review, Vol. 15, Issue 4, p. 26-30, 2021.

UNIVERSITY REVIEW

DEPENDENCE OF APPROXIMATION WITH THE MAXIMUM DESIGN PRESSURE TO THE YIELD STRENGHT OF THE MATERIAL AND THE APPLICABILITY OF VARIOUS TYPES OF CALCULATIONS TO THE MINIMUM SAFETY WALL THICKNESS OF THE GUN BARREL, CALCULATIONS FOR CALIBER 50BMG

Miroslav Polášek[1*] – Matúš Danko[2]

[1]Department of Mechanical Desing and Special Technology, Faculty of Special Technology, Alexander Dubček University of Trenčín, Ku kyselke 469, 911 06 Trenčín, Slovakia, E-mail address: miroslav.polasek@tnuni.sk
[2]Department of Mechtronics and Electronics, FEIT, University of Zilina, Univerzitná 8215/1, 010 26 Žilina, Slovakia, E-mail address: matus.danko@feit.uniza.sk

ARTICLE INFO

***Article history*:**
Received
Received in revised form
Accepted

Keywords:
gun barrel
barrel strength
yield strength
pressure in the barrel

Abstract:

For every weapon system, safety is essential for the users. The security of small caliber weapons is associated to the firing sequence. The danger spots are the closing mechanism and its fortress of fire. Another essential safety feature of the use of small caliber weapons is the correct oversizing of the gun barrel of both standard and tormentational ammunition, especially in the case of a shot. And in this work, we will deal with the correct calculations of the minimum wall thicknesses of the barrel.

1 Introduction

When designing a new gun barrel on a small caliber weapon, safety is essential. But usually there is the requirement for security and the least possible weight of the barrel, while these two requirements are in conflict. Of course, there are other important requirements if we need a barrel which, in addition to the required service life, has the best possible properties for the accuracy of long-distance shooting. It requires longer barrel as well as bigger outer diameter of the barrel. If we were designing a barrel for an automatic weapon, we would have to take into account the cooling of the barrel, what usually also means a further increase in outer diameters and also weight. When we set the requirements for what type of weapon, we are going to design the barrel, we have chosen repeating hunting rifle, repeating rifle for precision shooting "sniper rifle", semi auto or full auto. We have to rely on internal ballistics calculations. When we have internal ballistics diameters along the entire length of the barrel and the parameters of the material that we are going to use for the production of the gun barrel, we can use suitable types of calculations to determine the minimum averages in each part of the barrel.

2 Experimental details

To calculate internal ballistics, we used the QuickLOAD program, which calculates internal ballistics based on input data, which are:

- cartridge – .50 BMG (12.7x99 mm)/CIP standard,
- gun barrel length 800 mm (including cartridge chamber),
- gun powder type LOVEX D100, producer Explozia Pardubice (CZ),
- amount of gun powder 14.3 g = 220.7 grains/reloading tables Explozia Pardubice (CZ),
- total maximum cartridge length .50 BMG – 138.31 mm/CIP standard,

[*] Miroslav Polášek.
E-mail address: miroslav.polasek@tnuni.sk

- usable cartridge content .50 BMG – 15,809 cm3/QuickLOAD,
- bullet Hornady A-MAX 50cal. 750 grains/item 5165 Hornady.

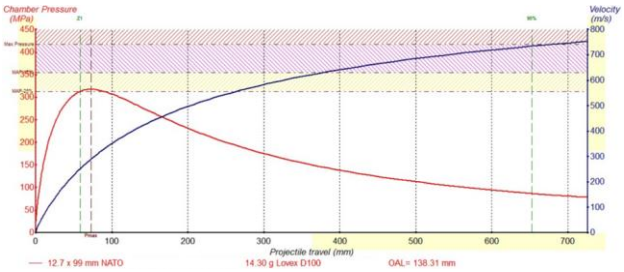

Fig. 1 Graphical representation of the course of pressure profile in the QuickLOAD program (red), the velocity of the projectile bottom (blue) and in the barrel (without the cartridge chamber) at 20 ° C

In Fig. 1, we can see a graph of the course of the barrel pressure in dependance on the barrel length, where is a sharp rise in pressure to maximum pressure and a gradual decline of the barrel pressure after reaching maximum. This graph also shows the acceleration of the projectile in the barrel depending on the length of the barrel. Speed and pressure are marked from the bottom of the projectile. The bottom of the projectile is 73.808 mm from the bottom of the barrel.

We made the calculation at the following places in the barrel:

- bottom of the cartridge chamber, inner diameter at least 20.52 mm, safety coef. k = 1.1, design pressure 529.1 MPa,
- cartridge case top, inner diameter at least 14.33 mm, safety coef. k = 1.1, design pressure 529.1 MPa,
- place of maximum pressure, inner diameter 13 mm, safety coef. k = 1.2, design pressure 577 MPa,
- place at the end of the barrel, inner diameter 13 mm, safety coef. k = 1.2 (safety coefficient at the end of the barrel is stated at least 2.5 in the literature [6], but since the condition of the minimum wall of the barrel is 2.5 mm, this condition of the safety coefficient is exceeded many times), design pressure 123.24 MPa, or at least the thinnest wall 2.5 mm, because the calculated size is usually smaller.

3 Results and discussion

Demonstration of each type of calculation of a simple unstrengthen barrel at material strength Re = 1100 MPa

3.1 Method 1. Calculation performed in the flexible area with sample calculation, according to the authors M. Fišer and S. Procházka, at Re = 1100 MPa

Dynamic value of yield strength:

- at Re = 1100 Mpa
- the calculated value is σ_{KD} = 1133 Mpa
- p = p_k – inner pressure

$$\alpha = \left(\frac{\sigma_{KD}}{p_K} \right)^2$$

- at p_k = 529.10 MPa the calculated value of the coefficient α = 4.59
- at p_k = 577 MPa the calculated value of the coefficient α = 3.86
- at p_k = 123.24 MPa the calculated value of the coefficient α = 84.52

$$x = \sqrt{\frac{\alpha + \sqrt{4\alpha - 3}}{\alpha - 3}}$$

- at p_k = 529.10 MPa, x = 2.315
- at p_k = 577 MPa, x = 2.936
- at p_k = 123.24 MPa, x = 1.123
- d_{2MN} – minimum outer diameter of the barrel
- r_1 – inner radius of the barrel
- d_1 – inner diameter of the barrel

$$d_{2MN} = d_1 \sqrt{\frac{\alpha + \sqrt{4\alpha - 3}}{\alpha - 3}}$$

$$d_{2MN} = d_1 \, . \, x$$

P.č.	r_1 (mm)	d_1 (mm)	d_{2MN} (mm)	α	x	p (MPa)
1	10,40	20,80	47,52	4,59	2,32	529,1
2	7,165	14,33	33,18	4,59	2,32	529,1
3	6,50	13,00	38,18	3,86	2,94	577,0
4	6,50	13,00	14,60	84,52	1,12	123,24

Fig. 2 Calculated minimum outer diameters of the barrel by Method 1 at Re = 1100 MPa

This method is suitable for calculation when there is a big difference between the design pressure and the pressure of the yield strength of the material. The yield strength is much higher than the design pressure, that is when the value of the coefficient α is much more than 3. If the coefficient α is close to 3, the calculated values are unrealistically large. This can be eliminated by replacing the material with a better material with higher yield strength:

$$\sigma_{red}{}^{I} = \frac{2}{3} \cdot \frac{2.x^2 + 1}{a^2 - 1} \cdot p_1$$

- where $a = r_2/r_1$ and $x = r_2/r$,
- r_1 – inner radius of the barrel,
- r_2 – outer radius of the barrel,
- r – radius of the barrel at the point of calculation,
- σ_{red} = stress according to maximum elongation,
- $p = p_1$ – inner pressure.

When calculating the minimum wall thickness of the barrel, the yield strength will not be exceeded further than 0.5 mm from the inside of the barrel wall.

P.č.	r_1 (mm)	r_2 (mm)	d_{2NDV}(mm)	r (mm)	$r-r_1$ (mm)	a	x	p (MPa)	s_{red} (MPa)
1	10,40	18,60	37,20	10,90	0,50	1,79	1,71	529,1	1094,77
2	7,165	12,50	25,00	7,665	0,50	1,74	1,63	529,1	1090,68
3	6,50	12,00	24,00	7,00	0,50	1,85	1,71	577,0	1098,53
4	6,50	7,22	14,44	7,00	0,50	1,11	1,03	123,24	1099,07

Fig. 3 Calculated minimum outer diameters of the barrel by Method 1 at Re = 1100 MPa

In this method, according to the theory of the maximum elongation, it follows that the reduced stress on the inner surface of the wall is less (or underestimated compared to the real pressure) than in the shear stress method (at higher pressures). At lower pressures, the opposite is true.

3.2 Method 2. According to the author J. Škvarek, the theory of the maximum elongation with a sample calculation at Re = 1100 MPa [13]

The tension of a simple gun barrel is solved under the assumption of a plane tension of the barrel wall (the tension in the prolonged direction is zero), due to the static pressure load of the gas. The relations for calculating the wall tension of the barrel derived from these assumptions give results that are sufficient for both strength control and wall thickness design. If we assume that the barrel will be loaded only by the inner pressure p_1, then the reduced stress according to the theory of the maximum elongation is determined from the relation:

$$\sigma_{red}{}^{I} = \frac{2}{3} \cdot \frac{2.x^2 + 1}{a^2 - 1} \cdot p_1$$

- where $a = r_2/r_1$ and $x = r_2/r$,
- r_1 – inner radius of the barrel,
- r_2 – outer radius of the barrel,
- r – radius of the barrel at the point of calculation,
- σ_{red} = stress according to maximum elongation,
- $p = p_1$ – inner pressure.

When calculating the minimum wall thickness of the barrel, the yield strength will not be exceeded further than 0.5 mm from the inside of the barrel wall.

P.č.	r_1 (mm)	r_2 (mm)	d_{2NDV}(mm)	r (mm)	$r-r_1$ (mm)	a	x	p (MPa)	s_{red} (MPa)
1	10,40	18,60	37,20	10,90	0,50	1,79	1,71	529,1	1094,77
2	7,165	12,50	25,00	7,665	0,50	1,74	1,63	529,1	1090,68
3	6,50	12,00	24,00	7,00	0,50	1,85	1,71	577,0	1098,53
4	6,50	7,22	14,44	7,00	0,50	1,11	1,03	123,24	1099,07

Fig. 4 Calculated minimum outer diameters of the barrel by Method 2 at Re = 1100 MPa

In this method, according to the theory of the maximum elongation, it follows that the reduced stress on the inner surface of the wall is less (or underestimated compared to the real pressure) than in the shear stress method (at higher pressures). At lower pressures, the opposite is true.

3.3 Method 3. According to the authors J. Pech and F. Kozderek with sample calculation at Re = 1100 MPa [10]

$$R = r \cdot \sqrt{\frac{k + 0{,}4.p}{k - 1{,}3.p}}$$

Formula for calculating the minimum wall thickness:

- R – outer radius,
- r – inner radius,
- $p_k = p$ – inner overpressure,
- k – allowable stress (yield strength).

P.č.	r (mm)	d_{2MN} (mm)	p (MPa)
1	10,40	36,75	529,1
2	7,165	27,89	529,1
3	6,50	25,17	577,0
4	6,50	14,36	123,24

Fig. 5 Calculated minimum outer diameters of the barrel by Method 3 at Re = 1100 MPa

This method is very practical. With this method it is possible to calculate favourable results, even if the results of other methods are already really unusable values (meaning very big minimum outer averages, which can no longer be used in practice). This method shows that it is older, from the war period, when the designers could quickly verify in practice what they calculated, and thus created more effective empirical methods than just theoretical way.

re=1100MPa, min. diameter method	diameter 20,8 mm Pk 529,1 MPa	diameter 14,33 mm Pk 529,1 MPa	diameter 13 mm Pk 577 MPa	diameter 13 mm Pk 123,24 MPa
1 [mm]	47,65	33,18	38,18	14,60
2 [mm]	40,00	27,60	27,60	14,80
3 [mm]	36,75	27,89	25,17	14,36
max. [mm]	47,65	33,18	38,18	14,80
min. [mm]	36,75	27,60	25,17	14,36
diameter difference max-min [mm]	10,90	5,58	13,01	0,44
radius difference max-min [mm]	5,45	2,79	6,51	0,22
difference max-min [%]	29,66	20,22	51,69	3,06

Fig. 6 Results of outer diameters of walls at Re = 1100 MPa, calculated by all methods

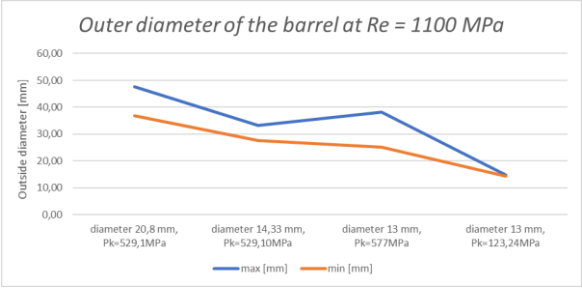

Fig. 7 Outer diameter of the barrel at Re = 1100 MPa

re=900MPa, min. priemery method	diameter 20,8 mm Pk 529,1 MPa	diameter 14,33 mm Pk 529,1 MPa	diameter 13 mm Pk 577 MPa	diameter 13 mm Pk 123,24 MPa
1 [mm]	99,99	69,83	N	14,95
2 [mm]	53,00	36,40	40,80	15,02
3 [mm]	47,15	36,31	35,46	14,74
max. [mm]	99,99	69,83	40,80	15,09
min. [mm]	47,15	36,31	35,46	14,65
diameter difference max-min [mm]	52,84	33,52	5,34	0,44
radius difference max-min [mm]	26,42	16,76	2,67	0,22
difference max-min [%]	112,07	92,32	15,06	3,00

Fig. 8 Results of outer diameters of walls at Re = 900 MPa, calculated by all methods

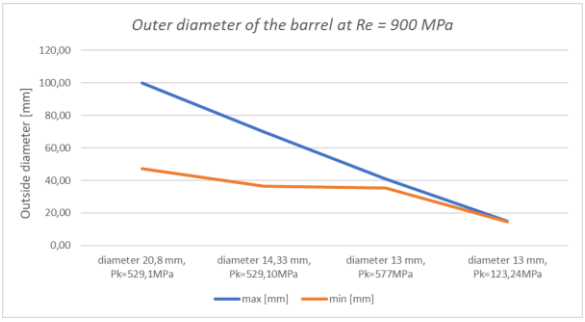

Fig. 9 Outer diameter of the barrel at Re = 900 MPa

re=800MPa, min. diameter method	diameter 20,8 mm Pk 529,1 MPa	diameter 14,33 mm Pk 529,1 MPa	diameter 13 mm Pk 577 MPa	diameter 13 mm Pk 123,24 MPa
1 [mm]	N	N	N	15,18
2 [mm]	72,80	50,20	82,00	15,32
3 [mm]	61,84	43,03	58,79	15,01
max. [mm]	72,80	65,17	82,00	15,32
min. [mm]	61,84	50,20	58,79	15,01
diameter difference max-min [mm]	10,96	14,97	23,21	0,31
radius difference max-min [mm]	5,48	7,49	11,61	0,16
difference max-min [%]	17,72	29,82	39,48	2,07

Fig. 10 Results of outer diameters of walls at Re = 800 MPa, calculated by all methods

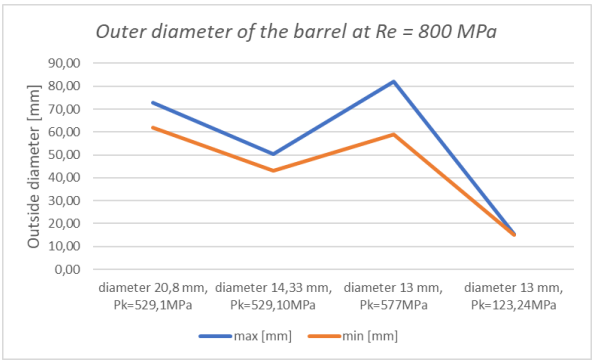

Fig. 11 Outer diameter of the barrel at Re = 800 MPa

4 Conclusion

When calculating the minimum wall thicknesses of the gun barrel, we must mainly take safety into account. Although other parameters are also essential when calculating the minimum wall thicknesses of the barrel for the standard cartridge where the maximum usable pressures are lower. For example, up to 200-300MPa, even with the inclusion of the reserve and when using standard barrel materials such as ČSN 15142 or ČSN 15230, there is no problem with calculating the minimum wall thickness of the barrel. This is because the yield strength of the material is much bigger than the maximum usable pressures at which the barrel is loaded during firing. If we design a gun barrel where the maximum usable pressures are higher than 300Mpa, with the standard usage of cartridge, there is a problem with calcula-

tions using standard materials such as ČSN 15142 or ČSN 15230. The design of a safe minimum wall thickness of the barrel requires materials with a higher yield strength while maintaining the minimum impact toughness. There are also problems in calculating the minimum wall thicknesses of the barrel, especially if the yield strength of the material is approaching the maximum usable pressures in the barrel. This is also seen in our work.

With a yield strength of 1100MPa, there was no problem to calculate the minimum diameters in each part of the barrel by all three methods. At a yield strength of 900MPa, there was no problem to calculate the minimum diameters in each part of the barrel by Methods 2 and 3, but Method 1 had a problem in calculating the minimum wall thickness of the barrel at a pressure of 577MPa and an inside diameter of 13mm. With a yield strength of 800MPa, there was no problem to calculate the minimum diameter in each part of the barrel by Methods 2 and 3, but Method 1 no longer gave us any result. Based on this work, calculation Methods 2 and 3 are more suitable when calculating the minimum required walls of the gun barrel. The best method is the method marked as number 3. At the smallest wall thicknesses, it also provides us with good safety. From our own experience we can write that even though this method calculates the smallest wall thicknesses, it provides sufficient security for the user of the weapon.

References

[1] BINDER, R. 1966. *Mechanika 3*. Bratislava : Slovenské Vydavateľstvo Technickej Literatúry, 1966. 416 s.

[2] FIŠER, M. 2003. *Malorážové zbraně. Základy konstrukce, U-1172*. Brno : Vojenská akademie v Brně, 2003. 360 s.

[3] FIŠER, M. – BALLA, J. 2004. *Malorážové zbraně, konstrukce, U-1377*. Brno : Univerzita obrany, 2004. 399 s. ISBN 8085960796.

[4] FIŠER, M. – LIPTÁK, P. – PROCHÁZKA , S. – MACKO, M. – JOZEFEK, M. 2006. *Automatické zbrane: Konštrukcia skúšanie, 1. vyd*. Trenčín : Trenčianska univerzita Alexandra Dubčeka v Trenčíne, 2006. 263 s. ISBN 80-8075-089-0.

[5] FIŠER, M. – POPELÍNSKÝ, L. 2004. *Malorážové zbraně: Konstrukce*. Brno : Univerzita obrany, 2004. ISBN 80-85960-79-6.

[6] FIŠER, M. – PROCHÁZKA, S. 2007. *Projektovaní loveckých, sportovních a obranných zbraní*. Ostrava : Vysoka škola báňská, 2007. 142 s.

[7] LEIGH, N. 2016. *Modern Snipers*. 2016. ISBN 9781472815347.

[8] LOBAEV, V. 2010. *The Sharpshooting*. 2010. ISBN 9785902073727.

[9] LILJA, D. – LILJA, S. 2020. *Barrel Lengths & Velocities for the 50 BMG*. [online]. Dostupné na internete: https://riflebarrels.com/barrel-lengths-velocities-for-the-50- bmg/

[10] PECH, J. – KOZDERKA, F. 1953. *Poznámky o konstrukci automatických zbraní*. Praha : Konštrukta Praha, 1953.

[11] POLÁŠEK, M. 2020. *Ideový návrh jednoranovej odstreľovacej pušky kaliber .50 BMG*. Diplomová práca. Trenčín : 2020. 91 s.

[12] POPELÍNSKÝ, L. 2000. *Projektování automatických zbraní: Výpočet funkčního diagramu automatické zbraně, 1. vyd*. Brno : Vojenská akadémia, 2000. 118 s.

[13] ŠKVAREK, J. 1995. *Hlavňové zbraně, část 4. Hlavně*. Brno : Vojenská akademie v Brně, 1995. 73 s.

[14] VAŠÍČEK, M. 1985. *Hlavně palných zbraní, U-34*. Brno : Vojenská akademie Antonína Zápotockého, 1985, 438 s.

University Review, Vol. 15, Issue 4, p. 30-36, 2021.

UNIVERSITY REVIEW

TESTING OF BATTERIES USED IN ELECTRIC CARS EVALUATION OF THE SMALLEST POSSIBLE CURRENT REQUIRED TO TEST THE FAULTS OF THE TRACTION BATTERY GRID

Miroslav Polášek[1*] – Milan Jus[2] – Matúš Danko[3]

[1]Department of Mechatronics and Electronics, FEIT, University of Zilina, Univerzitná 8215/1, 010 26 Žilina, Slovakia, E-mail address: polasek@stud.uniza.sk
[2]Department of Mechanical Desing and Special Technology, Faculty of Special Technology, Alexander Dubček University of Trencin, Ku kyselke 469, 911 06 Trenčín, Slovakia, E-mail address: milan.jus@tnuni.sk
[3]Department of Mechtronics and Electronics, FEIT, University of Zilina, Univerzitná 8215/1, 010 26 Žilina, Slovakia, E-mail address: matus.danko@feit.uniza.sk

ARTICLE INFO

***Article history*:**
Received: 26.11.2021
Received in revised form: 7.12. 2021
Accepted: 13.12.2021

Keywords:
battery charging
battery discharge
battery capacity
battery load
discharge current, power

Abstract:

The presented article presents the parameters of batteries used in electric cars. Measurements were performed for different types of batteries. The process of charging and subsequent discharging of these batteries took place. Different types of loads were used to discharge the batteries to find the smallest possible load current, which identifies the faults of the battery grid.

1 Introduction

Lithium-ion batteries have been used successfully in everyday life, from 3C products to EV (Electric vehicle), etc. If we introduce a newly developed lithium-iron phosphate (LiFePO4) battery with greater energy capacity and safer chemical properties, it was considered an excellent source of energy. Identifying damaged battery cells is therefore a topic that needs to be addressed in order to eliminate the additional costs associated with using the battery.

The main reason for the widespread expansion of lithium cells is the low rate of self-discharge, high capacity and relatively high specific energy. Due to the growing demand of industry for reliable, high-energy and small-scale energy sources. The decisive feature in lithium cells is in particular the energy density, which depends on the material of the electrodes. In *Fig. 1* is a comparison of energy density and specific energy of current cells with older types of batteries. In comparison, there is a lead-acid battery, nickel-cadmium, nickel-metal hydride, lithium polymer and lithium ion. From the graphical interpretation we can see that the li-ion battery has the highest specific energy and energy density. [1]

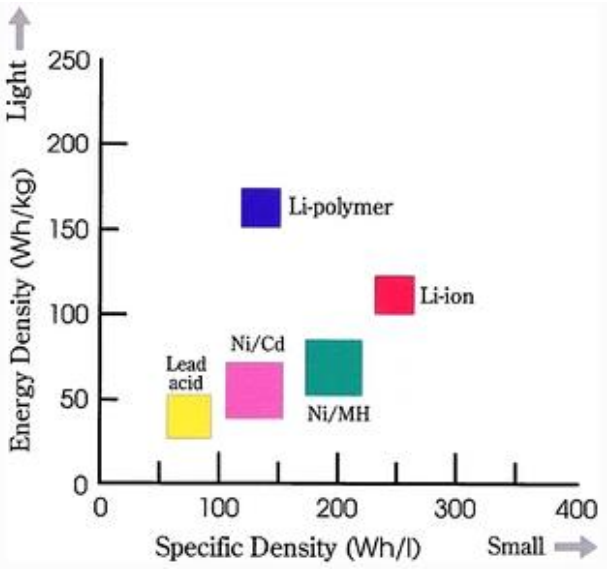

Fig. 1 Energy density versus specific density diagram for various types of batteries [1]

* Miroslav Polášek.
E-mail address: polasek@stud.uniza.sk

Initially, lithium batteries were produced as primary batteries, a type of battery that cannot be recharged. During electrochemical, the substances needed to generate electricity were consumed. Oxidation-reduction processes are irreversible and gassing and possible electrolyte leakage occurs when recharging. The advantages of primary cells are high energy density, low weight and relatively low cost due to single use.

The first secondary types of lithium cells encountered problems such as overheating and explosions. From a safety point of view, it was necessary to replace lithium metal with a less aggressive material. In 1991, Sony introduced a rechargeable lithium cell consisting of a graphite anode and a cathode of cobalt oxide. [2]

Lithium-ion batteries vary in terms of the internal structure material used. They acquire specific properties based on the use of a combination of selected materials for the anode, cathode and separator. The electrolyte is formed through a lithium salt. The intercalation process is the basic principle for the operation of a lithium-ion cell. Intercalation electrodes are composed of compounds that allow lithium ions to be embedded in the crystal lattice of another substance. The host structure into which the ion has been placed through intercalation will change. The result is an intercalating compound called an intercalate. The intercalation process is chemically or thermally reversible.

During operation, lithium-ion batteries are exposed to an aging process that results in a loss of cell capacity and performance. *Table 1* shows the effects of processes on article parameters.

Table 1 Influences of processes on article parameters

Process	Effect	Influence	Cause
Electrolyte decomposition	Loss of lithium Increase in internal impedance	Decrease in capacity Decrease in power	High temperatures High State of Charge (SOC)
Solvent intercalation, gassing and subsequent cracking in particles	Loss of active material and lithium	Decrease in capacity	Overcharging
Reduction of the surface area due to the continued formation of the Solid Electrolyte Interface (SEI) layer	Increase in internal impedance	Decrease in power	High temperatures High SOC
Changes in porosity due to volume changes, SEI layer formation	Increase in internal impedance Surplus potentials	Decrease in power	High cycling rate High SOC
Loss of active material particles due to volume changes during cycling	Loss of active material	Decrease in capacity	High cycling rate High Depth of Discharge (DOD)
Binder decomposition	Loss of lithium Loss of mechanical stability	Decrease in capacity	High temperatures High SOC

The cathode material is one of the most expensive parts of the lithium-ion battery and significantly affects the final price. The cathode materials are prepared in a discharged lithium state (when they contain lithium atoms) so that they can be paired with anodes that do not contain lithium atoms. When maximizing energy density, it is important that the potential between the cathode and anode material is as high as possible. This requirement limits the choice of cathode materials to transition metal compounds such as manganese, iron, cobalt and nickel. Oxides and polyanionic compounds of transition metals are also used for cathode materials.

Cathode materials must meet the following requirements [19]:

• Ability to intercalate large amounts of lithium

• Ability to deintercalate lithium without structural changes
• High energy value
• High potential due to lithium
• Compatibility with other materials in the article
• Insolubility in the electrolyte
• Low preparation costs
• Good electron conductivity

Over time, many electrode materials have been developed and subsequently studied, which are still commercially available today. Most of the investigated commercially available cathode materials contain a layered structure ($LiNiO_2$, $LiCoO_2$). Unlike previous materials, $LiMn_2O_4$ has a spinel structure. This material is important in the commercial sphere because it does not fall under the Mizuchimov and Goodenough patent of 1981. The patent only applies to oxide compounds that have a layered structure. [3]

In terms of time, we can divide the cathode materials into:
• First generation ($LiNiO_2$, $LiCoO_2$)
• Second generation ($LiFePO_4$, $LiMn_2O_4$, $LiNi_{1-x}Co_xO_2$, $LiMnO_2$, $LiMn_{1-x}Co_xO_2$, $LiNi_{1-x}Mn_xO_2$, $LiNi_{1-x-y}Mn_xCo_yO$)
• Third generation ($LiCoPO_4$, $LiNi_{0.5}Mn_{1.5}O_4$)

Table 2 Cathode materials and their basic parameter differences [3]

Material	Structure	Average voltage potential versus lithium [V]	Theoretical specific capacity [mAh/g]
$LiCoO_2$	Layered	3.88	130-160
$LiNiO_2$	Layered	3.55	200
$LiMn_2O_4$	Spinel	4.10	100-130
$LiFePO_4$	Olivine	3.45	140-170

2 Experimental details

Zhidou D1 electric car batteries were used for the measurement. The complete battery pack of the vehicle is composed of cells, type LiFePo4. The capacity of each cell is 150Ah. The battery pack has been used for about 6 years on the vehicle. We used three types of loads for the measurement. The first load is 15A, which is 0.1C. The second load is 60A, which is 0.4C. The third load is 120A, which is 0.8C. The measurement was made from a minimum current of 15A to a current of 120A. The voltage ranges used on the batteries were based on the values of how the batteries are used by the vehicle. We set the minimum value of the battery voltage during the measurement to 2.8V, because the vehicle switches off the entire battery pack if the voltage on any cell drops below 2.8V (with or without load). We set the highest voltage on the cell to 3.60V. For the measurement, we used a load from Chroma ATE Inc., model 63203E-150-300.

3 Results and discussion

3.1 Measured results of load 15A – 0.1C

Load 15A – 0.1C, battery 3144-14

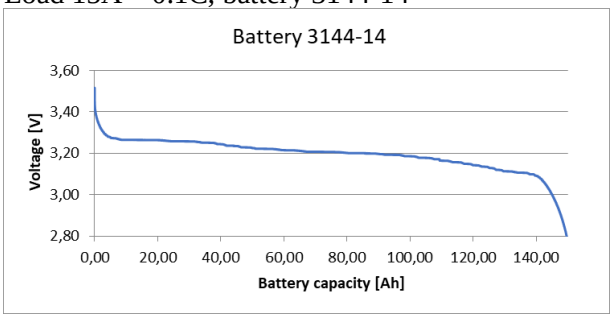

Fig. 2 The course of voltage on the battery 3144-14 at a load of 0.1C, final battery capacity 145.57Ah

Load 15A – 0.1C, battery 3144-15

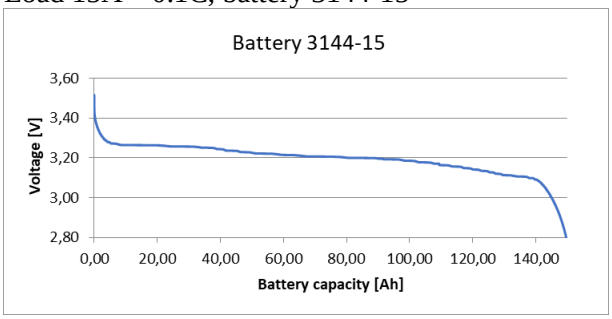

Fig. 3 The course of voltage on the battery 3144-14 at a load of 0.1C, final battery capacity 146.01Ah

Load 15A – 0.1C, battery 3618-14

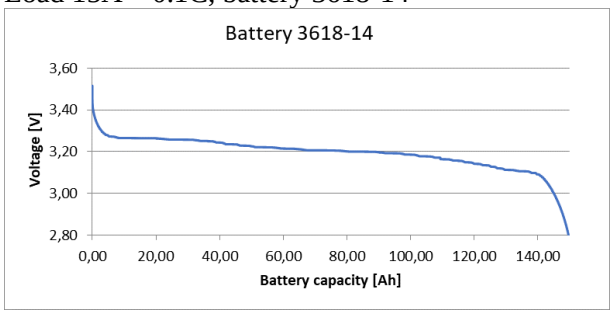

Fig. 4 The course of voltage on the battery 3618-14 at a load of 0.1C, final battery capacity 148.65Ah

Load 15A – 0.1C, battery 3618-16

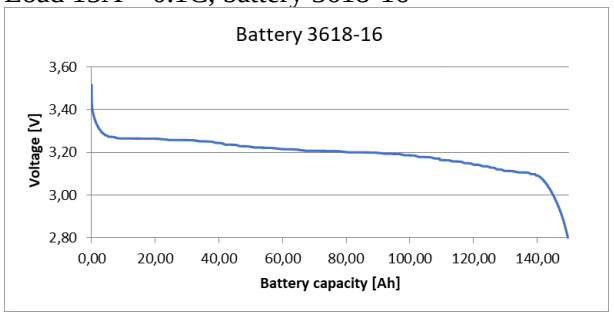

Fig. 5 The course of voltage on the battery 3618-16 at a load of 0.1C, final battery capacity 149.62Ah

3.2 Measured results of load 60A – 0.4C

Battery 3144-14

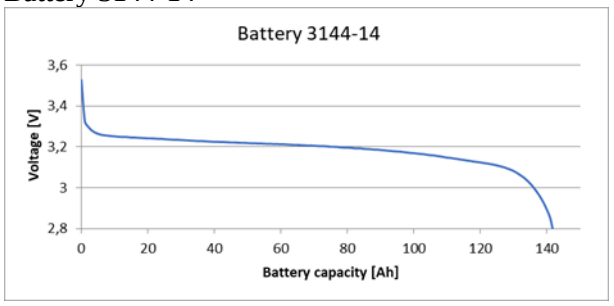

Fig. 6 The course of voltage on battery 3144-14 at load 0.4C, final battery capacity 141.76Ah

Battery 3144-15

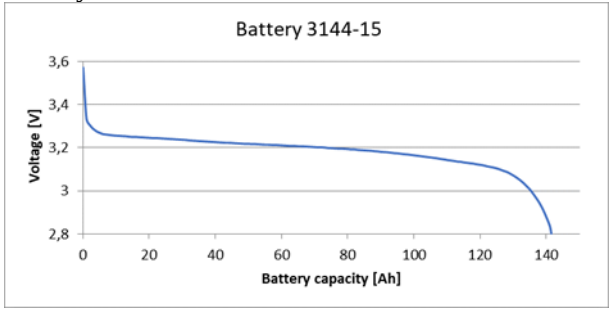

Fig. 7 The course of voltage on battery 3144-15 at load 0.4C, final battery capacity 141.46Ah

Battery 3618-14

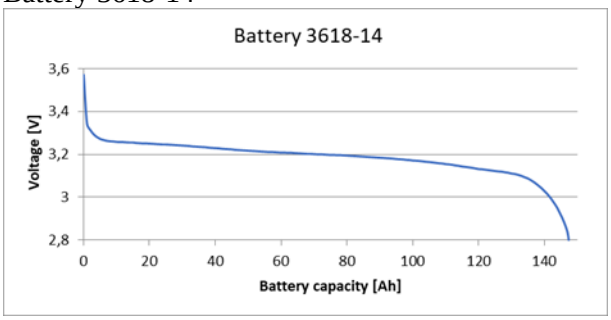

Fig. 8 The course of voltage on the battery 3618-14 at a load of 0.4C, final battery capacity147.38Ah

Battery 3618-16

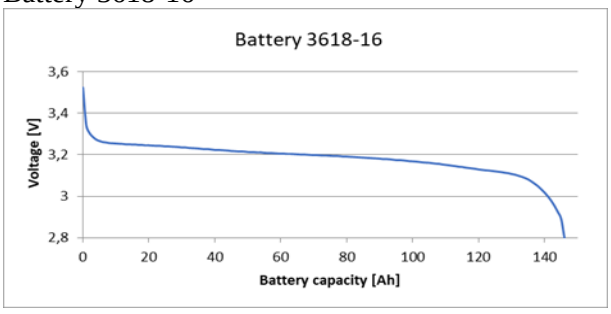

Fig. 9 The course of voltage on the battery 3618-16 at a load of 0.4C, final battery capacity 146.00 Ah

3.3 Measured results of load 120A – 0.8C

Battery 3144-14

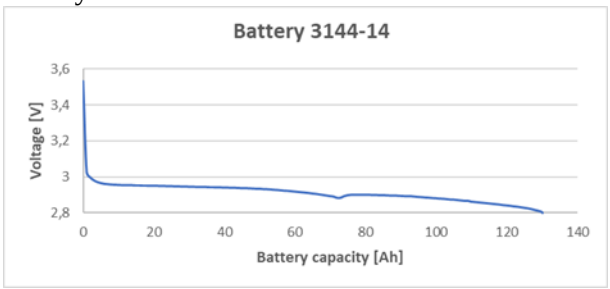

Fig. 9 The course of voltage on the battery 3144-14 at a load of 0.8C, final battery capacity 130.20 Ah

Battery 3144-15

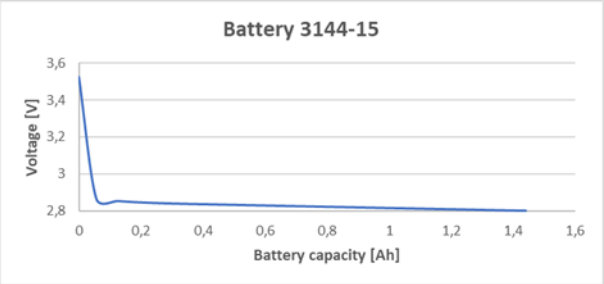

Fig. 10 The course of voltage on the battery 3144-15 at a load of 0.8C, final battery capacity 1.44Ah

Battery 3618-14

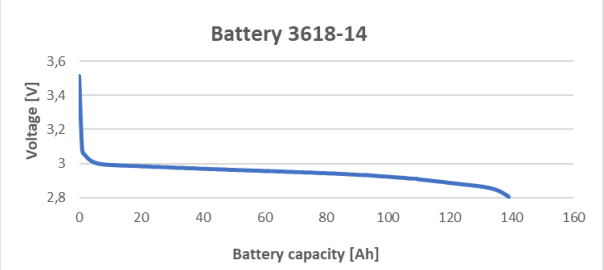

Fig. 11 The course of voltage on the battery 3618-14 at a load of 0.8C, final battery capacity 139.10Ah

Battery 3618-16

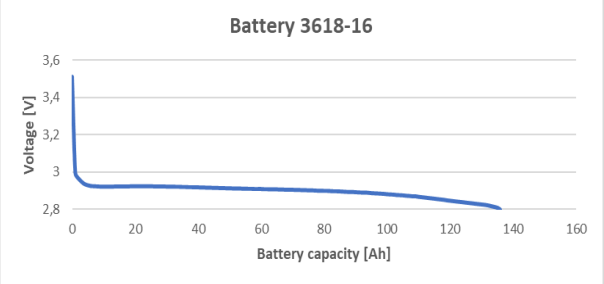

Fig. 12 The course of voltage on battery 3618-16 at load 0.8C, final battery capacity 135.82Ah

Table 3 Table of measured values of battery capacities at different loads and their percentage evaluation

Battery name	3144-14	3144-15	3618-14	3618-16
Capacity of battery, load 0,1C [Ah]	145,57	146,01	148,65	149,62
Capacity from the original capacity [%]	97,05	97,34	99,10	99,75
Decrease in capacity from the original capacity [%]	2,95	2,66	0,90	0,25
Capacity of battery, load 0,4C [Ah]	141,76	141,46	147,38	146
Capacity from the original capacity [%]	94,51	94,31	98,25	97,33
Decrease in capacity from the original capacity [%]	5,49	5,69	1,75	2,67
Capacity of battery, load 0,8C [Ah]	130,2	1,44	139,1	135,82
Capacity from the original capacity [%]	86,80	0,96	92,73	90,55
Decrease in capacity from the original capacity [%]	13,20	99,04	7,27	9,45

We measured a capacity of 145.57Ah for the 3144-14 battery with a load of 0.1C = 15A, which is only 2.95% less than the value of the new battery. At a load of 0.4C = 60A, we measured a value of 141.76Ah, which is 5.49% below the value of the new battery. At a load of 0.8C = 120A, we measured a value of 130.20 Ah, which is 13.20% below the value of the new battery. This battery is still good for use in a vehicle.

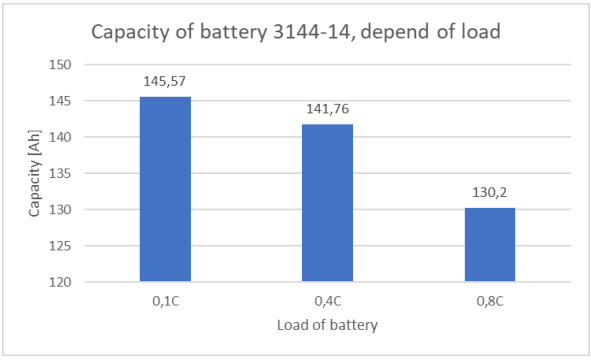

Fig. 13 Description of the measured value of capacities on the battery 3144-14

We measured a capacity of 146.01Ah for the 3144-15 battery with a load of 0.1C = 15A, which is only 2.66% less than the value of the new battery. At a load of 0.4C = 60A, we measured a value of 141.46Ah, which is 5.69% below the value of the new battery. At a load of 0.8C = 120A, we measured a value of 1.44Ah, which is 99.04% below the value of the new battery. This battery cannot be longer used in the vehicle, the 0.8C current is standardly used when operating the vehicle. A 0.8C load revealed a faulty internal grille.

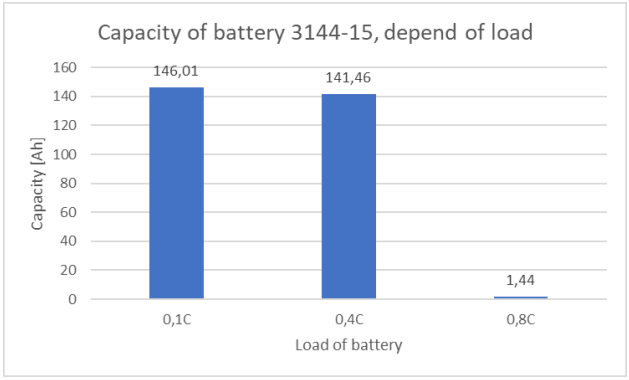

Fig. 14 Description of the measured value of capacities on the battery 3144-15

We measured a capacity of 148.65Ah for the 3618-14 battery with a load of 0.1C = 15A, which is only 0.90% less than the value of the new battery. At a load of 0.4C = 60A, we measured a value of 147.38Ah, which is 1.75% below the value of the new battery. At a load of 0.8C = 120A, we measured a value of 139.1Ah which is 7.27% below the value of a new battery. This battery has small differences

from the new battery and it is still good for use in a vehicle.

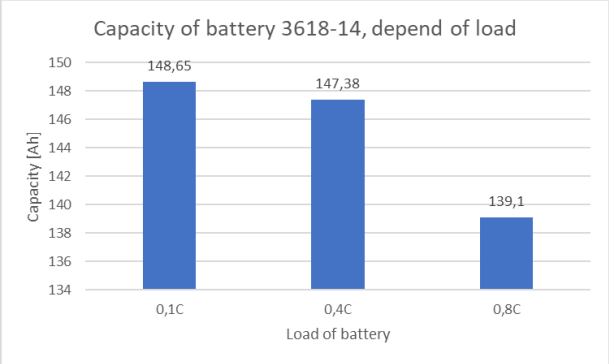

Fig. 15 Description of the measured value of capacities on the battery 3618-14

We measured a capacity of 149.62Ah for the 3618-16 battery with a load of 0.1C = 15A, which is only 0.25% less than the value of the new battery. At a load of 0.4C = 60A, we measured a value of 146.00Ah, which is a value of 2.67% below the value of the new battery. At a load of 0.8C = 120A, we measured a value of 135.92Ah which is 9.45% below the value of a new battery. This battery has small differences from the new battery and it is still good for use in a vehicle.

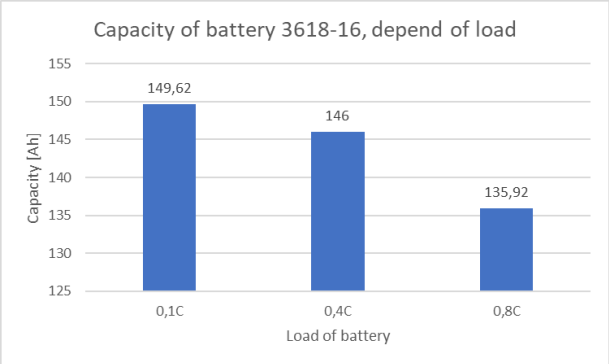

Fig. 16 Description of the measured value of capacities on the battery 3618-16

4 Conclusion

When testing the battery, we found small differences in capacity from 0.25 to 2.95% compared to the value of the new battery when 0.1C (15A in this case) load was applied. These differences did not indicate a problem when using these batteries, if the battery is charged 0.4C, a current of 60A. The differences in the measured capacity are higher from 1.75 to 5.69% compared to the capacity of the new battery. Although the differences in measured capacity are 2.74% higher than the lower load, the batteries are still alright for normal use in the vehicle. When the battery loading is 0.8C with a current of 120A, the differences in the measured capacity are higher from 7.27 to 99.04% compared to the value of the new battery. A difference of 99.04% compared to the new battery capacity means only 0.96% capacity of the original capacity. This difference is very high so we have found a faulty battery which cannot be used longer in the vehicle. The result is that we need to use a minimum load of 0.8C to detect faulty batteries. Perhaps in the future, after measuring multiple batteries, we will find the dependence how to find the faulty battery even at a lower load such as 0.8C, based on multiple measurements and finding new dependencies between the lower load and the faulty battery. Even on our measurement, we can see the highest decrease in measured capacity when loading 0.4C is compared to the new capacity of the battery. The measured decrease of 5.69% on the battery 3144-15 confirmed the damage on the battery when the load was higher.

References

[1] Scrosati, B.: *History of lithium batteries.* Journal of Solid State Electrochemistry, Berlin/Heidelberg: Springer-Verlag, 0110n. l., 15(7): 1623- 1630 DOI: 10.1007/s10008-011-1386-8. ISSN 1432-8488.

[2] SONY: *Corporate Info – Chapter 13 Recognized as an International Standard.* [22.11.2021], Online: http://www.sony.net/SonyInfo/CorporateInfo/History/SonyHistory/2-13.html

[3] Reddy, T. B., Linden D.: *Linden's handbook of batteries.* 3rd edition, 1454 s., New York: McGraw-Hill, 2001. ISBN 0-07-135978-8.

[4] Adamec, J., *VÝSKUM MOŽNOSTÍ ZVYŠOVANIA SPOĽAHLIVOSTI A BEZPEČNOSTI ZÁSOBNÍKOV ENERGIE V ELEKTROMOBILOCH*, 2019, DIZERTAČNÁ PRÁCA

[5] Jonathan S.: *Reliability Characterisation of Electrical and Electronic Systems*, 2014, ISBN 9781782422211.

[6] Yoo, H. D., Markevich, E., Salta, G., Sharon, D., Aurbach, D., *On the challenge of developing advanced technologies for electrochemical energy storage and conversion*. Materials Today 2014, ISSN 1369-7021.

University Review, Vol. 15, Issue 4, p. 37-42, 2021.

UNIVERSITY REVIEW

INVESTIGATION OF MICROSTRUCTURE AND STRENGTH PROPERTIES OF INTERFACE BETWEEN INCONEL 625 WELD LAYER AND 16Mo3 STEEL

Patrik Klučiar*[1] – Michal Krbaťa[1] – Igor Barényi[1] – Ján Palkech[2]

[1]Department of Mechanilcal Engineering Technologies and Materials, Faculty of Special Technology, Trenchiniensis Univeritas of Trencin, Ku kyselke 469, 911 06 Trencin
[2] Konštrukta Defence, a.s., Lieskovec 575/25, Dubnica nad Vahom.

ARTICLE INFO

***Article history*:**
Received: 26.11. 2021
Received in revised form: 7.12. 2021
Accepted: 13.12. 2021

Keywords:
Weld
Tensile test
Microstructure

Abstract:

The article deals with the investigation of weld Inconel 625 layer low alloyed heat resistant 16Mo3 steel. The investigation was focused on the analysis of the behavior of the layer during the load by tensile strength test including strength properties evaluation of the layer – substrate system. The microstructure of the system was investigated too with a focus on the interface between layer and the substrate.

1 Introduction

Components of heating devices, used for the extraction of waste energy, which works in the most aggressive environments, are usually made by high alloyed high temperature resistant steel or low or medium alloyed with used a high temperature resistant layers and welds. Nowadays, weld layers of nickel based alloys are used to achieve high temperature resistance. Nickel alloy Inconel 625 is frequently used in this process, due to its very good high corrosive durability, even at high temperature, good creep resistance, and good weldability too [1,2].

During the technological welding process, a specific layer of primary material (steel) melts and then is mixed with covering metal in the welding bath. Between primary material and weld coating so-called transitional are ais created (Fig. 1).
The transitional area is the area where are primary and welding materials are mixed. The chemical composition, microstructure and properties of primary material in this zone are changing smoothly by distance from the weld material [3,4]. The width of the transition zone is a function of the chemical composition of the primary metal and the weld, the method of welding, the heat input, as well as the feed rate of the cover wire [5,6].

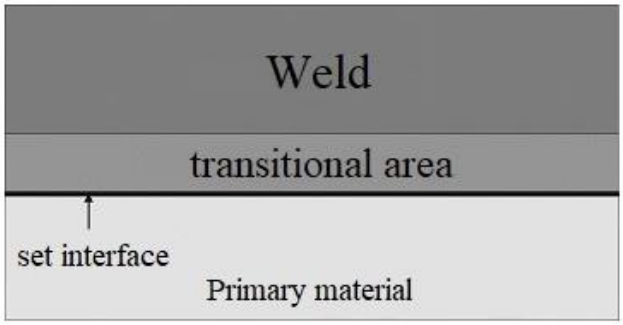

Fig. 1Microstructure zones in weld layer [1]

2 Materials and methods

2.1 Experimental materials

Base material (substrate) is the low alloyed steel for use at softly elevated temperature – 16Mo3 (tab. 1). Inconel 625 (tab. 2) was selected as a weld layer thanks to its very good corrosion resistance even at high temperatures, good creep resistance also weldability. The thicknesses of the weld and the base material are in ratio 3: 7,

* Corresponding author. Tel.: +421 915 423 281
E-mail address: patrik.kluciar@tnuni.sk

where the weld with higher mechanical properties acts as a bearing element and the resulting yield strength of the whole system is higher as the tensile strength of the base material.

Tab. 1 Basic chemical composition and mechanical properties of 16Mo3 steel

Material	Steel 16Mo3			
wt.%	Min.	Max.	Tensile strength R_m [MPa]	440
C	0,1	0,2		
Mn	0,5	0,8	Yield point $R_{p0,2}$ [MPa]	380
SI	0,15	0,37		
Al	--	0,015	Ductility A [%]	30
P	--	0,04		
S	--	0,04	Hardness HV	150
Fe	Bal.			

Tab. 2 Basic chemical composition and mechanical properties of Inconel 625alloy used for experiment

Material	Inconel 625 (NiCr22Mo9Nb)			
wt.%	Min.	Max.	Tensile strength R_m [MPa]	965
Cr	20	23		
Mo	8	10		
Co	--	1		
Nb	3,15	4,15	Yield point $R_{p0,2}$ [MPa]	490
Ti	--	0,4		
Fe	--	5		
C	--	0,1		
Mn	--	0,5	Elongation(at 20 °C) A [%]	50
Si	--	0,5		
Al	--	0,4		
P	--	0,015	Hardness HV5 (before cold rolling)	200
S	--	0,015		
Ni	Bal.			

Fig. 2 Microstructure of primary material - 16Mo3 steel

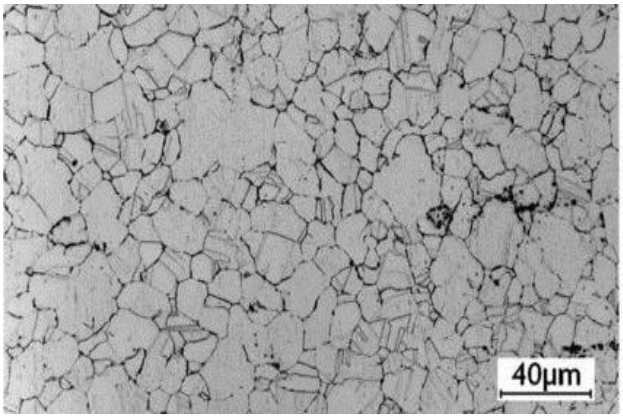

Fig. 3 Microstructure of Inconel 625

The microstructure of the primary material (16Mo3 steel) is shown in Fig. 2. It is a ferrite-perlitic structure consisting of ferrite grains with perlite on their borders. Furthermore, it is possible to observe fine precipitated carbides at or near the grain boundaries. The microstructure of Inconel 625 is in Fig. 3. It is a simple homogenous structure based on grains of γ phase with randomly distributed fine precipitates.

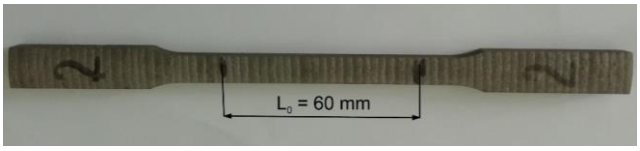

Fig. 4 Testing sample for tensile test

The shape of the test sample, used for performed static tensile test is in Fig. 4. Basic dimensions of the samples, then used for calculation of mechanical characteristics are listed in table 1.

Tab. 3 Basic dimensions of samples

Label of sample	Thickness [mm]	Width [mm]	Cross section S_0 [mm^2]	L_0 [mm]
1	6,1	8	48,8	60
2	6,1	8	48,8	60

Inconel coating was applied using Ar shielding gas. Tubes were cooled with water flow (10 l/min) through their inside during the process. The thickness of the clad layers was approximately 2,5 mm [7,8].

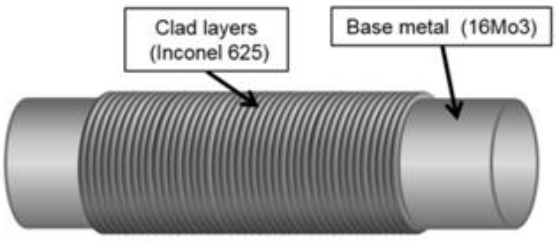

Fig. 5 Schematic illustration of tubes of16Mo3 steel with Inconel 625 welding overlay

2.2 Tensile strength test

The static tensile test is prescribed by EN ISO 6892-1 standard. The principle of the test is the static loading of the test sample by tensile stress to its fracture. The sample must have a standardized shape and size. The sample axis and axis of applied force are in coincidence. The stress-strain curve is then measured as a basis for strength mechanical characteristics evaluation from its characteristic points tensile strength, yield point etc.). From the size of the sample before and after the test is possible to calculate plasticity characteristics (ductility, contraction) [9].

The experimental sample consists of a combination of alloy Inconel 625 weld on 16Mo3 steel. Both materials have significantly different mechanical properties. The tensile strength of the alloy Inconel 625 is at an ambient temperature almost double compared to 16Mo3 steel. Measured mechanical characteristics are a certain combination of the properties of both mixed materials. Both materials also differ in yield point nature. At ambient temperature, Inconel 625 has a non-visible yield point in the stress-strain curve, but 16Mo3 steel yield point is visible. For that reason, the yield strength values of experimental samples were evaluated by the methodology for the determination of contractual yield strength (proof stress) [9].

3 Experimental results

3.1 Strength properties

Tensile strength, yield strength and ductility of test samples were evaluated by tensile strength test. The resulting experimental values are listed in table 4. Yield strength was evaluated as proof stress of 0,2%, because materials Inconel 625 have non-visible yield point in ambient temperature, while 16Mo3 steel point is visible in the stress-strain curve.

Tab. 4 Experimental results from the tensile test

Label of sample	R_m [MPa]	$R_{p0,2}$ [MPa]	A_{60}[%]
1	573,70	425,02	35
2	577,55	430,10	32
average	575,62	427,56	33

The corresponding stress strain curve obtained from the tensile test of samples no. 1 is in Fig. 6 as an example.

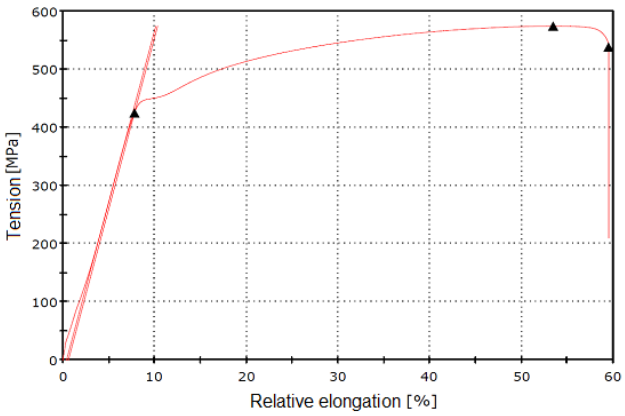

Fig. 6 Strass-strain curve for sample 1

Sample with weld consists of two homogeneous materials. The basic mechanical characteristics of the weld (Inconel 625) are significantly higher as the characteristics of steel 16Mo3. Their mutual comparison with values of the sample with weld, which was obtained by experiment, is in Fig. 7.

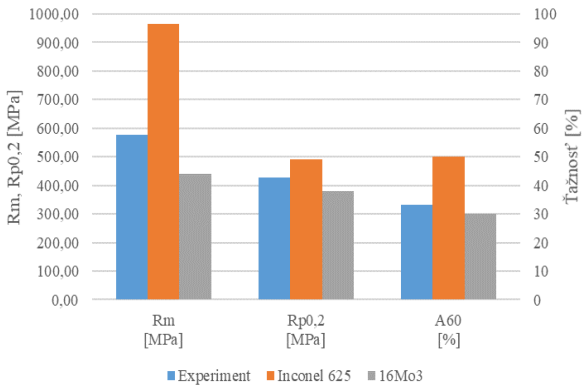

Fig. 7 Mutual comparison mechanical characteristics of basic material, weld and experimental sample with weld

Inconel 625 has very high plastics properties (ductility) and relatively low hardness. For this reason, any cracking was not observed during the experiment at any stage of the loading. For this reason, no cracking or other damage mechanism and separation of the layer from the base material was observed at any stage of the sample loading during the test, which is characteristic of e.g. for very hard nitrided layers.Although the thickness of the weld and base material is in ratio 3:7, the weld with higher mechanical properties acts as a supporting element and the resulting yield strength of the whole system is higher than the tensile strength of the base material itself. The failure of the entire cross-section of the sample occurred at the 30% higher stress value than the tensile strength of the base material itself. The total tensile strength of the experimental sample does not reach the tensile strength of the Inconel 625 alloy at the ambient temperature. After fracture the base material, there will be a significant reduction in the sample cross-section, which at the same acting load means a significant stress increase. This stress is higher as the tensile strength of Inconel 625 alloy. Therefore, the layer breaks immediately after the damaging of base material and total fracture of the sample occurs.

3.2 Microstructural analysis of primary material

General view of the interface weld layer – basic material is shown in Fig. 8. The interface is formed by three basic areas, which are at the figure marked as A, B and C. Areas A and B form a transition area, whereas C is the basic material. A more detailed view of the first section (A) is in Fig. 9. This is the area of partial or complete melting, where the basic material has been heated to the area of stable austenite above temperature A_1. After the welding, there was a rapid cooling, therefore martensite needles are visible in the structure together with ferrite grains. Perlit of original ferritic-perlitic structure austenitized during heating of the material and subsequent rapid cooling caused its martensitic transformation. Temperature of heating was not high enough for the overall reverse transformation of ferrite to austenite and because of this, original ferritic grains are also visible in the structure.

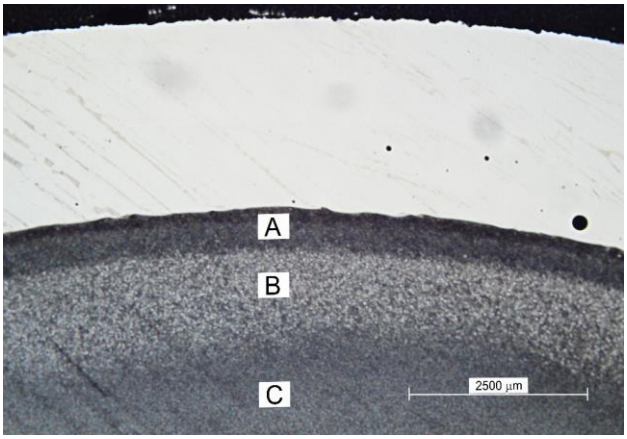

Fig. 8 General view on basic material and weld interface and his three basic areas

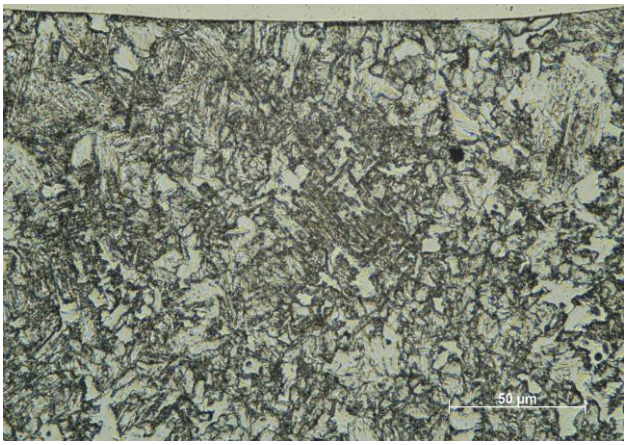

Fig. 9 Interface of weld - basic material-melting zone (A)

Figure 16 shows the more detailed view of the second part of the interface of weld – basic material (B). This is an area of overheating where the material has not melted, but only has been heated to temperatures below A1 and subsequently held at this temperature as the electrode passes over the surface during welding. Structure in this area didn't undergo phase transformation but significant coarsening ferrite grains has occurred. At the ferrite grain boundaries, perlite and carbides are segregated.

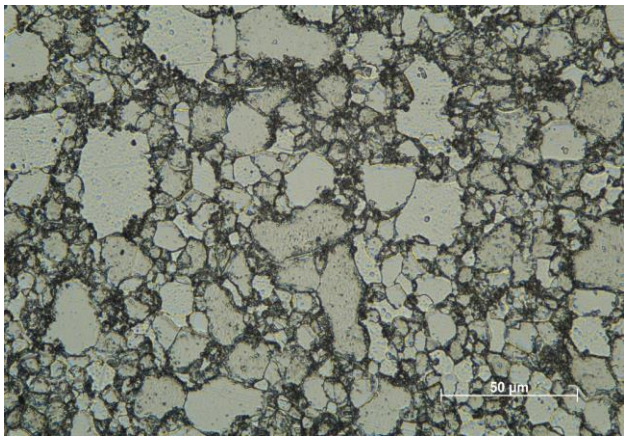

Fig. 10 Interface of weld - basic material-overheating zone (B)

4 Conclusion

The subject of the research was a weld of heat resistant alloy Inconel 625 on primary material 16Mo3 steel. The first part is focused on weld layer behavior during tensile loading as well as mechanical properties of Inconel coated samples. The second part deals with the microstructure investigation of the interface between the overlay and the substrate. The experiments can be concluded as follow:

- Strength properties of the system are approximately 30% higher than properties of primary material (16Mo3).
- Due to the high plastic properties, the weld did not crack during the tensile test until the rupture.
- The microstructure of the interface can be divided into three zones. Zone with partial melting where the martensite was observed with preserved ferritic grains. The overheated zone without phase transformation but with grain coarsening. The third zone corresponds with the base material structure.

5 Acknowledgement

This publication was created in the frame of the project: Advancement and support of R&D for "Centre for diagnostics and quality testing of materials" in the domains of the RIS3 SK specialization, ITMS2014+:313011W442, based on the Operational Programme Integrated Infrastructure and funded from the European Regional Development Fund.

6 References

[1] X. Xing, X. Di, B. Wang, The effect of post-weld heat treatment temperature on the microstructure of Inconel 625 deposited metal,J. Alloys Compd. 593, 110-116 (2014).

[2] S.A. David, J.A. Siefert, J.N. DuPont, J.P. Shingledecker, Weldabillityand weld performance of candidate nickel base superalloys for advanced ultra supercritical fossil power plants part I: fundamentals, Sci. Technol. Weld. Joining. **7**, 532-550 (2015).

[3] J.C. Lippold, Welding Metallurgy and Weldability, A John Wiley& Sons, Inc, New Jersey, 2015.

[4] J.N. DuPont, J.C. Lippold, S.D. Kiser, Welding Metallurgy and Weldability of Nickel-Base Alloys, A John Wiley & Sons, INC., Publication, 2009.

[5] J.N. DuPont, Microstructural evolution and high temperature failure of ferritic to austenitic dissimilar welds, Int. Mater. Rev.**4**, 208-232 (2012).

[6] J.N. DuPont, C.S. Kusko, Technical Note: Martensite formation in austenitic/ferritic dissimilar alloy welds, Weld. J. 51-54 (2007).

[7] EN 10028-2, FlatProducts Made of SteelsforPressurePurposes - Part 2: Nonalloyand alloySteelswithSpecifiedElevatedTemperatureProperties, vol. 3,2000.

[8] SpecialMetalsCorporation, Corporation-informationmaterials, http://www.specialmetals.com/assets/smc/documents/alloys/inconel/inconel-alloy-625

[9] I. Barenyi, M. Ličková: Náuka o materiáloch II, FŠT TnUAD, Trenčín 2015, ISBN 978-80-8075-689-5

[10] M.D. Rowe, T.W. Nelson, J.C. Lippold, Hydrogen-induced cracking along the fusion bound-

ary of dissimilar metal welds, Weld.J., 31-37 (1999).
[11] A.A. Omar, Effects of welding parameters on hard zone formation at dissimilar metal welds, Research Developments, 86-93 (1998).
[12] B. Zhihui Wang, B. Xu, C. YE, Study of the martensite structure at the weld interface and the fracture toughness of dissimilar metal joints, Weld. Res. Suppl. 397-402 (1993).
[13] C.C. Silva, H.C. de Miranda, M.F. Motta, J.P Farias, Influence of welding in operational conditions on the partial mixed zone formation in Ni-based dissimilar weld overlay, Trends in welding research, The Materials Information Society pp. 336-344, 2012.
[14] B.T. Alexandrov, J.C. Lippold, J.W. Sowards, a. T. Hope, D.R.Saltzmann, Fusion boundary microstructure evolution associated with embrittlement of Ni-base alloy overlays applied to carbon steel, Weld World **57**, 39-53 (2012).
[15] G. Li, J. Huang, Y. Wu, An investigation on microstructure and properties of dissimilar welded Inconel 625 and SUS 304 using high-power CO2 laser, Int. J. Adv. Manuf. Technol. **76**, 1203-1214(2015).
[16] M. Rozmus-Górnikowska, M. Blicharski, J. Kusiński, L. Kusiński,M. Marszycki, Influence of boiler pipe cladding techniques on theirmicrostructure and properties. Arch. Metall. Mater. **58**, 1993-1996(2013).
[17] M. Rozmus-Górnikowska, M. Blicharski, J. Kusiński, MetalicMaterials **52**, 141-147 (2014).